Langmuir
Invited Feature Article
pubs.acs.org/Langmuir

# Probing of Polymer Surfaces in the Viscoelastic Regime

Marius Chyasnavichyus, Seth L. Young, and Vladimir V. Tsukruk*

School of Materials Science and Engineering, Georgia Institute of Technology, Atlanta, Georgia 30332, United States

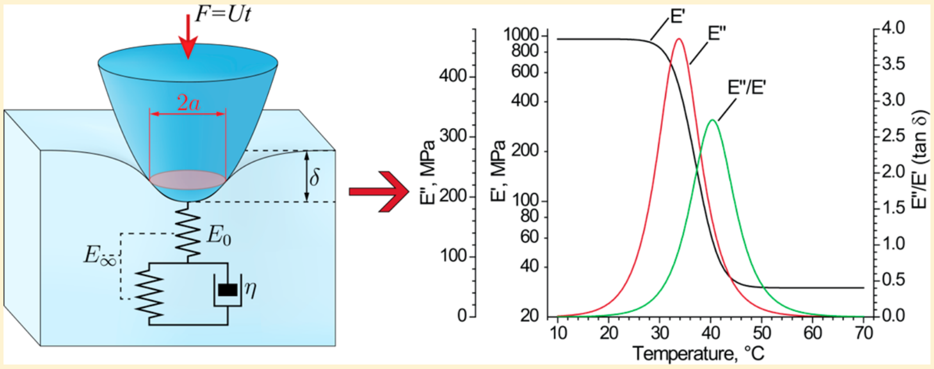

**ABSTRACT:** In this Feature Article, we discussed the experimental and modeling methods and analyzed the limitations of the surface probing of nanomechanical properties of polymeric and biological materials in static and dynamic regimes with atomic force microscopy (AFM), which are widely utilized currently. To facilitate such measurements with minimized ambiguities, in this study we present a combined method to evaluate the viscoelastic properties of compliant polymeric materials. We collected force−distance data in the static regime for a benchmark polymer material (poly(*n*-butyl methacrylate)) with an easily accessible glass-transition temperature (about 25 °C) at different loading rates and different temperatures across the glassy state, glass-transition region, and rubbery state. For this analysis, we exploited a Johnson-modified Sneddon's approach in a combination with the standard linear solid model. Critical experimental steps suggested for robust probing are (i) the use of a tip with a well-characterized parabolic shape, (ii) probing in a liquid environment in order to reduce jump-in phenomenon, and (iii) minute indentations to ensure the absence of plastic deformation. Whereas the standard Sneddon's model generates quantitatively adequate elastic modulus values below and above the glass transition, this traditional approach can significantly underestimate actual modulus values in the vicinity of the glass-transition region (15 °C above or below $T_g$), with major deviations occurring at the loss tangent peak. The analysis of the experimental data with Sneddon's model for the elastic region (glassy and rubbery states) and Johnson's model for the viscoelastic region allowed for the restoration of the universal master curve and the evaluation of the storage modulus, loss modulus, loss tangent, relaxation times, and activation energies of the polymer surface across the glass-transition region and at relevant loading rates.

## ■ INTRODUCTION

Measurements of micromechanical properties on thin polymer films, organic coatings, biological materials, and polymer surfaces with traditional tools such as dynamic mechanical analysis, nanoindentation, bulging, and buckling is a challenging task because of a range of unfavorable circumstances including modest strain and stress sensitivities, substrate contributions, insufficient local deformation, and poor control of minute deformations and forces.[1] Therefore, a version of atomic force microscopy (AFM), usually called surface force spectroscopy (SFS), is widely exploited because it allows high-resolution measurements of force, position, and deformation even if precise contact mechanics behavior frequently remains debatable.[2] During the SFS measurements, an AFM tip is brought into intimate contact with the surface under investigation and is pressed into the material. The corresponding applied force versus tip displacement is measured in the form of so-called force−distance curves (FDCs).[3] From these direct measurements, surface deformation can be evaluated, and the elastic properties of materials can be calculated and mapped by assuming certain contact mechanics models of elastic deformation and avoiding plastic deformation.[4]

SFS probing has been successfully used for micromechanical measurements with a high spatial resolution of ultrathin soft materials such as homopolymers, polymer blends, polymer brushes, block copolymers, hydrogels, and individual molecules on various substrates, in liquid, and at various temperatures.[2,5,6] The AFM is capable of applying and detecting forces that are orders of magnitude lower than that of covalent bonds and comparable to weak interactions, making it a unique tool for probing intermolecular interactions.[7,8] The limitation of SFS is that it can probe only surfaces (or topmost sublayers and subsurfaces), as opposed to other approaches such as micro/nanoindentation that are capable of probing submicrometer- to

**Received:** December 23, 2013
**Revised:** February 8, 2014
**Published:** February 10, 2014

dx.doi.org/10.1021/la404925h | *Langmuir* 2014, 30, 10566−10582

micrometer-sized depths. The pull-off forces acting on the tip during SFS measurements are widely employed in studies of synthetic and protein macromolecular unfolding, brush layer stretching, and other tensile-related mechanical properties of individual molecules and usually require a modification of the tip surface with selective binding groups.[9−11]

Initial developments in SFS methods were devoted to the verification of the mathematical contact models of tip−sample interactions.[12] Various methods of data analysis were introduced to account for the tip shape (Sneddon's model),[37] tip−sample interactions (Derjaguin−Muller−Toporov (DMT), Johnson−Kendall−Roberts (JKR), and Maugis−Dugdale (MD),[13−15] and plastic deformations (Oliver−Pharr (OP) approach).[16] These developments exploited contact mechanics to study the complex deformational, elastic and plastic, tensile and compressive, and static and dynamic behavior of various compliant and hard surfaces.

However, even if plastic deformation, strong adhesive forces, and substrate contributions can be avoided or reduced during experimental routines, the major assumption of purely elastic deformation cannot necessarily be considered valid for inherently viscoelastic polymeric and biological materials. Indeed, at temperatures near the glassy-to-rubbery transition, $T_g$, the time-dependent behavior becomes dominant and viscoelastic materials can exhibit a dramatic decrease in storage modulus by as much as 3 orders of magnitude, which is accompanied by a dramatic increase in the loss modulus at temperatures slightly above the formal glass transition at a maximum loss tangent.[2,17−20] To analyze this complex phenomenon, significant efforts have been undertaken to develop AFM-based probing modes and corresponding data analysis approaches to determine the viscoelastic properties of materials with significant mechanical energy losses under various assumptions.[21,22]

Many of these current approaches are aimed at measuring the dissipative energy between the AFM tip and the polymer surface by exploiting dynamic force modulation techniques in which a phase lag of the oscillating AFM tip is used for the evaluation of the loss modulus under dynamic conditions.[23−25] In these dynamic methods, either the phase lag between the sample position and the response of the cantilever or the ratio of the damped cantilever amplitude versus its free air amplitude, $A/A_o$, are monitored during continuous surface mapping. The variations are directly interpreted in terms of the loss tangent, which corresponds to the ratio of dissipated energy (loss modulus, $E''$) to elastically stored energy (storage modulus, $E'$), $E''/E'$.[18,26] Although this approach can be useful when mapping the viscoelastic response of a material with high resolution, the unambiguous separation of $E'$ and $E''$ parameters requires a precise knowledge of cantilever dynamics, an additional calibration step for a reference sample with known elastic properties, and usually must be conducted at uncharacteristically high frequencies (up to MHz) that are not relevant to actual practical deformation rates of materials.[27,28]

Another popular AFM-based so-called static method allows for the study of the slow viscoelastic creep of polymeric and biological materials.[29] In the case of the AFM creep experiment, the constant mechanical load is applied to the sample surface and the resultant tip motion due to material relaxation is monitored over long time periods (from seconds to hours). Next, simple models that treat the measured sample as a combination of elastic springs and viscous dashpots are used to derive the viscoelastic properties from these stress-displacement data.[30] However, large plastic deformations are usually induced on the sample surface during the long-time measurements, which limits the applicability of the method, especially in the case of thin polymer coatings where mechanical properties depend strongly on the penetration depth and are affected by the supporting solid substrate.[26] In addition, the surface mapping of mechanical properties is extremely time-consuming under this approach and cannot be conducted with high spatial resolution. Also, such measurements require a force and position feedback loop, which displaces the base of the cantilever to accommodate sample relaxation and keep the force constant. Unfortunately, such a feature is not readily available on many commercial instruments.

Overall, further developments are required to fully utilize the capability of AFM operation for continuous, high-resolution, and nondestructive monitoring of the viscoelastic behavior of compliant materials. Therefore, in this Feature Article, we briefly discuss various methods of viscoelastic property evaluation that are based on FDC analysis with the tip approaching the sample at a constant rate in comparison to some other experimental approaches. We show that reliable SFS probing can be conducted in a wide range of relevant temperatures and frequencies with dramatically reduced capillary forces in order to determine the viscoelastic response of the sample surface without common distortions caused by plastic deformation, adhesive forces, supporting substrates, or high probing rates in a wide range of frequencies and with sufficient statistics. Such measurements can be practically made in the conventional surface force mapping mode.

In this experimental study, FDCs are analyzed by combining the standard Sneddon's contact mechanics model with the standard linear solid (SLS) viscoelastic model in Johnson's interpretation for indentation experiments to extract critical materials parameters such as the sample's instantaneous modulus ($E_0$), which represents the elastic modulus of the material at very fast loading rates, infinite modulus ($E_\infty$), which represents the elastic modulus of the material at substantially slow loading rates, and finally relaxation time ($\tau$), the time scale of polymer chain rearrangement with applied stress.[31] Furthermore, the micromechanical properties of the amorphous polymeric material selected here with a glass-transition temperature close to room temperature (Experimental Section) is analyzed by employing the time−temperature correspondence principle.[31] Such an approach allows for the reproduction of generalized time-dependent mechanical properties of viscoelastic polymeric materials such as global master curves, relaxation times, and activation energies in a wide temperature and frequency range around the glass transition.

## Basic SFS Probing Concepts Overview: Current Status.

*FDC Collection.* As opposed to general mechanical analysis techniques where stress is measured as a function of strain, in SFS experiments the data is usually analyzed in terms of the continuous penetration of the AFM tip into the material as induced by the near-normal load (so-called loading curves). These loading curves are derived from experimental FDCs in which cantilever deflection $d$ and position $z$ are directly measured while the tip moves toward (approaching curve) or away from (retracting curve) the surface, as presented schematically in Figure 1a.[32,33] For simplicity, here we define the contact point as the point where the AFM tip first touches the surface, with the actual definition of the contact point varying for different approaching conditions (e.g., with significant repulsive or attractive forces).

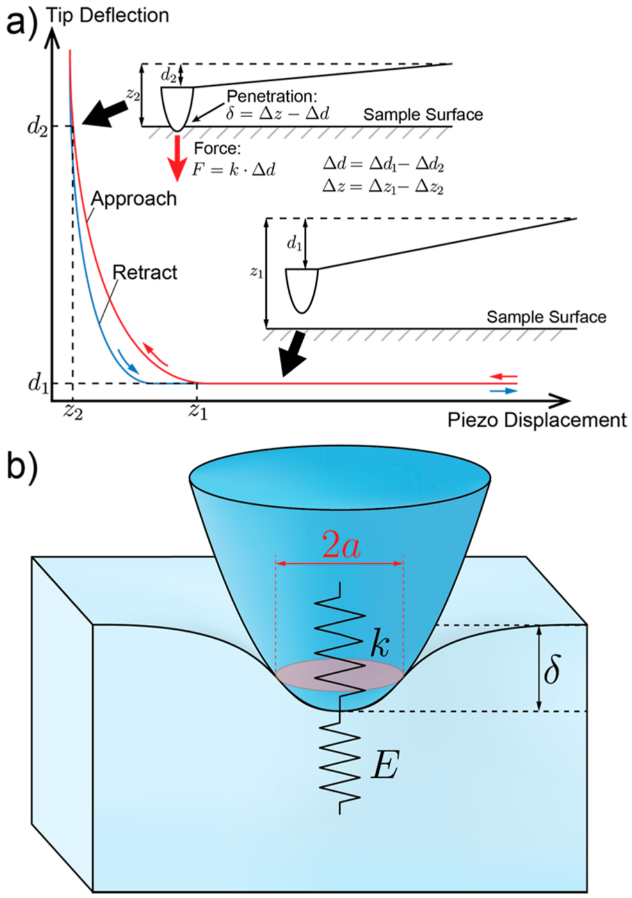

**Figure 1.** (a) Schematic representation of the tip−sample interaction and major parameters of the force−distance curve. (b) Schematics of Sneddon's model for axisymmetric hard punch pressed against a purely elastic material with modulus *E*.

The difference between the piezoelement displacement ($\Delta z$) and the cantilever deflection ($\Delta d$), $\delta = \Delta z - \Delta d$, is usually called penetration, and it accounts for the amount of the local deformation of the surface. It should be noted that because relative changes in both piezo displacement and tip deflection are used, different reference points can be chosen for both values. After the maximum deflection is achieved, the AFM tip is retracted (retracting curve) with some hysteresis usually observed as a result of energy dissipation and high adhesive forces.[34] Assuming purely elastic cantilever behavior (very low damping in air with $Q$ on the order of several hundred) with a spring constant $k$, the force exerted by the AFM tip on the surface, $F$, can be calculated from the measured cantilever deflection as $F = k\Delta d$, and this deformational behavior can be simply treated with a spring-against-spring model.[35]

*Tip–Surface Interactions.* The spring-against-spring approach usually includes the classical Hertzian model that describes small reversible deformations of compliant elastic semispheres pressed against each other.[36] However, in the most practical cases, the indenter is much harder than the studied material, thereby limiting the use of this classical model in indentation experiments, especially in cases that involve significant penetration depths. Therefore, Sneddon's model extended the contact mechanics theory by solving the problem of the indentation of an axisymmetric hard punch into an elastic half space with Young's modulus $E$ (Figure 1b).[37]

In this model, an indentor shape is described by the function $f(x)$ (to describe different shapes), and the hard punch makes a contact area with a circular plane projection of radius $a$ with the elastic material. Sneddon's analysis led to the analytical equations for the penetration $\delta$ and force $F$ exerted by the hard punch in the form[37]

$$\delta = \int_0^1 \frac{f'(x)}{\sqrt{1 - x^2}}\,\mathrm{d}x \tag{1}$$

$$F = 2\left(\frac{1 - \nu^2}{E}\right)a \int_0^1 \frac{x^2 f'(x)}{\sqrt{1 - x^2}}\,\mathrm{d}x \tag{2}$$

where $\nu$ is the sample Poisson ratio (usually assumed to be close to 0.5 for purely elastic deformation). Here and in the following discussion of indentation contact models, the punch is assumed to be rigid and not deformable.

Analytical solutions and deformational relationships for common indenter geometries are summarized in Figure 2. It can be seen that for the case of the spherical indenter there is no simple relation between the force and penetration. However,

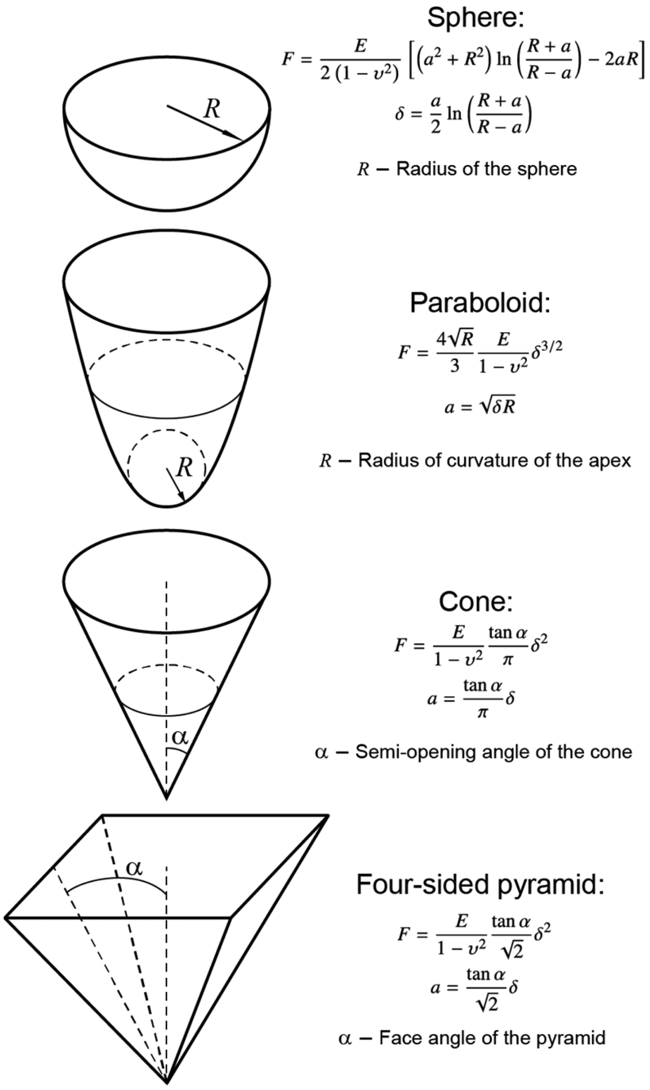

**Figure 2.** Sneddon's model equations for applied force $F$ and contact area with effective radius of contact $a$ for several common indenter shapes.

for the indenter of a parabolic shape, there is a simple equation that relates the penetration $\delta^{3/2}$ to the applied load in a linear manner. Because in the vicinity of the apex a spherical indenter can be approximated with a parabolic shape, the same linear relationship $\delta^{3/2}(F)$ can be used in the case of spherical indenters for penetrations that are much smaller than the radius of the sphere.

In the case of very soft surfaces such as that for living cells or very compliant hydrogels where during the indentation the tip penetrates deeply into the sample, the tip shape should be approximated by a cone as the area under the apex of the tip becomes small compared to the total contact area. Other relations are utilized as well, for example, in the case of AFM tips of well-defined pyramidal shape with a square base, which is important for large deformations.[38] Therefore, the Sneddon's model presents a universal solution to the indentation problem, which is not limited to spherical shapes and small indentations while providing analytical expressions for the penetration and load in the case of the hard indenter and the elastic sample.

*Surface Forces and Elastic Deformations.* One of the main limitations of the Sneddon approach is the fact that it does not account for the presence of surface forces (van der Waals or Coulomb) acting on the tip during mechanical contact and in the vicinity of the surfaces. These forces are evident from the appearance of jump-to-contact and jump-off-contact instabilities observed in FDCs in common SFS experiments.[32] The jump-to-contact phenomenon appears on the approaching part of the FDC as an instantaneous snap of the tip onto the sample surface when the surface forces exerted by the sample onto the tip exceed the restoring spring force determined by the cantilever spring constant. These surface forces exert an additional load on the tip−sample interface at the contact point and in the vicinity, therefore changing the initial force distribution, definition of the contact point, and penetration profile. Over the years, different models were established to account for this important effect.[34]

The first model describing the adhesive behavior was introduced by Bradley.[39] This model describes the contact between the two rigid spheres with no elastic deformation. The adhesive force, $F_{ad}$, acting between two spheres was estimated to be $F_{ad} = 2\pi R\gamma$, where $\gamma$ is the work of adhesion—the energy that is needed to separate two surfaces. Following this simplistic approach, two more complex models describing the deformable contact with the inclusion of adhesive forces were introduced: the DMT model[13] and the JKR model[14] (Figure 3a). In the DMT model, which was initially developed for the case of a soft sphere indented into a rigid half space, the deformed state of the tip−sample interface is not influenced by the presence of the attractive force. There, the only deviations from simplistic Hertzian behavior are additional long-range attractive surface forces acting outside of the contact region:

$$F_{ad} = 2\pi R\gamma \tag{3}$$

$$a = \sqrt[3]{\frac{3R(1-\upsilon^2)}{4E}(F + F_{ad})} \tag{4}$$

$$\delta = \frac{a^2}{R} \tag{5}$$

The alternative JKR model accounts for an additional deformation of the tip−sample interface, which is caused by the adhesive forces (Figure 3a). These forces act only at short range within the contact area, which is increased in comparison to that of the simple Sneddon's model and results in the following relationships:

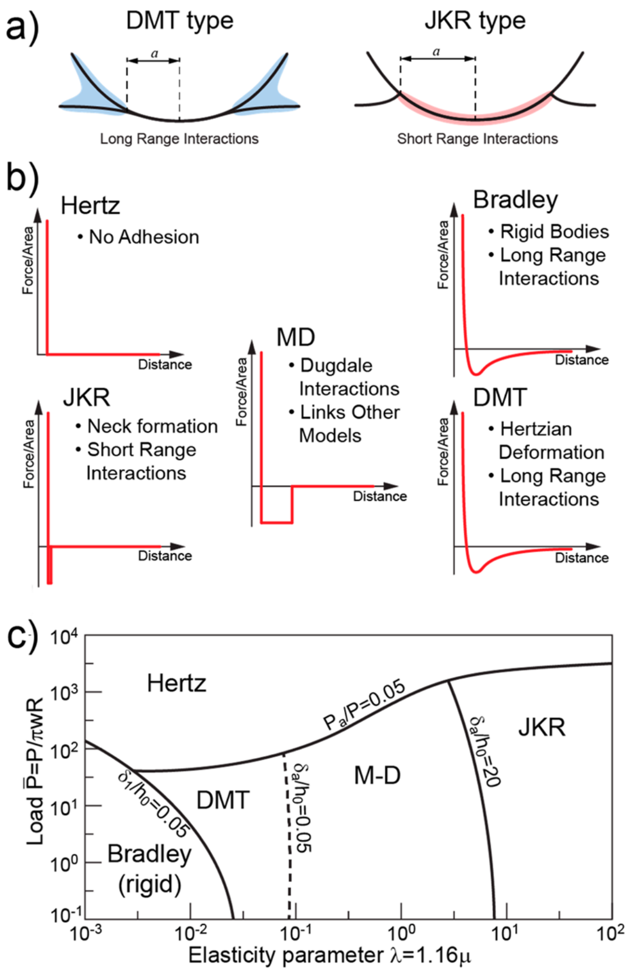

**Figure 3.** (a) Tip−sample interactions as presented by DMT and JKR models. (b) Interaction forces used in various contact mechanics models. (c) Adhesion map depicting the suggested ranges of applicability of various contact mechanics models.[41]

$$F_{ad} = \frac{3}{2}\pi R\gamma \tag{6}$$

$$a = \sqrt[3]{\frac{3R(1-\upsilon^2)}{4E}\left(F + 2F_{ad} + 2\sqrt{F_{ad}(F + F_{ad})}\right)} \tag{7}$$

$$\delta = \frac{a^2}{R} - \sqrt{\frac{4}{3}\frac{F_{ad}}{R}\frac{(1-\upsilon^2)}{E}a} \tag{8}$$

It should be noted that the penetration calculated with the JKR model can have negative values because of the adhesion of the sample surface to the tip, whereby upon tip retraction a physical neck can be formed between the indenter and the sample.[40] Because the JKR model completely neglects the long-range interactions and the DMT model does not account for the influence of the adhesive forces in the contact region, it is evident that neither model can fully describe the complete deformational behavior of the highly adhesive elastic materials.

Maugis presented the next MD model, which describes the limiting cases of the adhesive behavior of tip−sample interactions in the form of potential curves (Figure 3b).[15] Maugis introduced the potential as a step function, known as

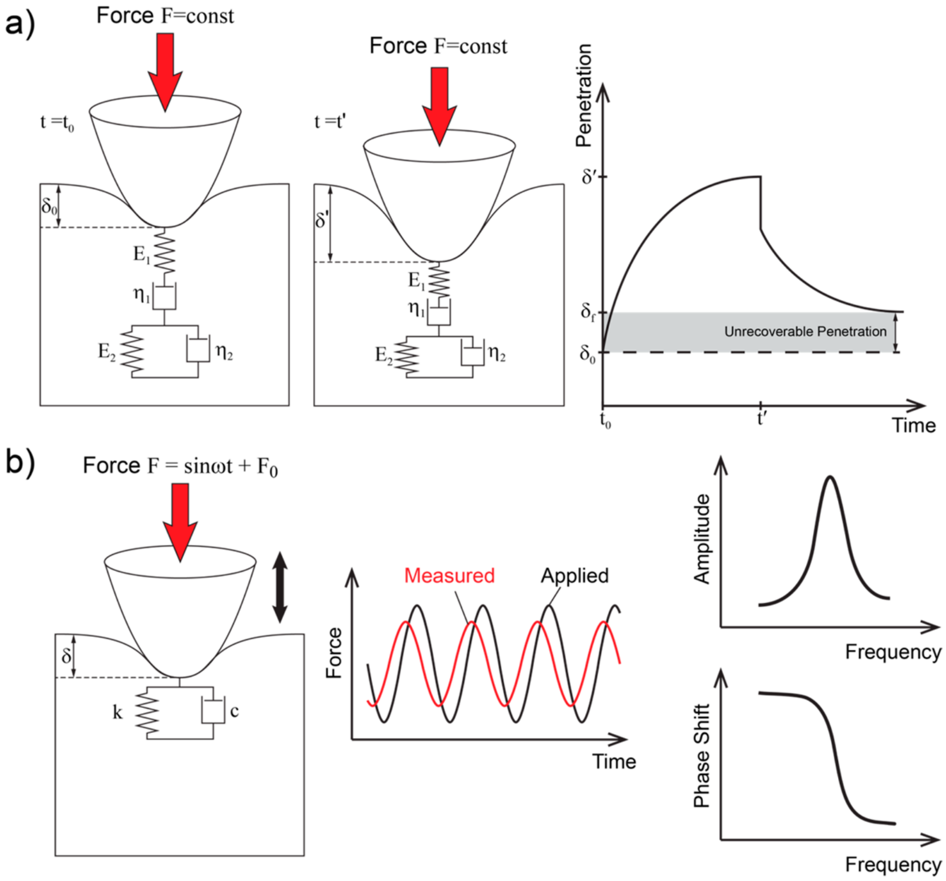

**Figure 4.** (a) Creep experiment for the material as analyzed by a four-element model and the resulting penetration vs time curve. (b) Contact force resonance measurements with dynamic indentation amplitude and phase shift plots.

the Dugdale potential. To describe the shape of this step function, the dimensionless parameter $\lambda$ (elasticity parameter) was introduced

$$\lambda = \frac{2.06}{z_0}\sqrt[3]{\frac{R\gamma^2}{\pi}\left(\frac{3}{4}\frac{(1-\upsilon^2)}{E}\right)^2} \tag{9}$$

where $z_0$ is the effective range of surface forces.

Parameter $\lambda$ can be shown to represent the ratio of the elastic displacement of the surface at the jump-off contact point, $\delta_a$, to the effective range of adhesive forces, $h_0$. Therefore, for large spherical indenters and compliant materials $\lambda \to \infty$, whereas for small indenters and stiff materials $\lambda \to 0$. By introducing an additional parameter that corresponds to the ratio of applied load to the effective adhesive energy, $\overline{F} = F/\pi\gamma R$, Johnson and Greenwood constructed a full adhesive map depicting the ranges of the applicability of various contact mechanics models for a particular experimental setup (corresponding schematics in Figure 3c).[41] For example, this map suggests that if the adhesive force at the jump-off contact point is less than 5% of the applied mechanical load then the simple Hertzian model describes the deformations in the contact region well (Figure 3c). Several additional models presented simplified approximations for the range of $\lambda$ parameters.[42,43]

*Plastic Deformation Role.* In SFS micromechanical measurements, hard indenters (AFM tips) typically have a small radius of curvature at the apex (10−20 nm), and hence only very small indentations can be performed before the material yields. The simplest way to estimate the yielding point for the material is to use Tabor's representative strain.[44] For the case of spherical and conical indenters, these limiting strains could be estimated as $\varepsilon = 0.2a/R$ and $0.2\cot(\alpha)$, respectively (assuming the same definitions used in Figure 2). A comparison of these values with the strain at the yield point gives a rough estimation of the transition between purely elastic and elastic−plastic regions of deformation.

If elastic−plastic deformation occurs, then the greatest challenge is the clear separation of elastic and plastic components of the deformation. Oliver and Pharr introduced a method for the evaluation of mechanical properties at large plastic deformations by separating the purely elastic regime.[16] The method concentrates on the earliest stages of the unloading (retracing) curve, where the restoring material behavior is assumed to be purely elastic and the contact area is well defined. At this point, the elastic modulus can be simply estimated from the slope of the FDC as[45]

$$E = \frac{1}{\beta}\frac{(1-\upsilon^2)}{2}\frac{\sqrt{\pi}}{\sqrt{A}} \tag{10}$$

where $A$ is the contact area and $\beta$ is a shape-indentor correction factor that is different for different indentors.

This method works very well for hard materials with small elastic strains such as metals and ceramics but has some limitations for use in soft polymeric systems with pronounced relaxations.[46] However, for soft polymeric materials, the pile-up effect significantly changes the contact geometry such that the contact area becomes unknown and cannot be easily used in the elastic modulus calculation. Then, the model does not account for additional adhesion and frequent long-neck formation, which is common in compliant and highly adhesive polymeric materials. The additional limitation is related to the time-dependent properties of the polymers that can cause the appearance of an apparent negative stiffness.[47] Therefore, for soft material, models that account for time-dependent mechanical properties and complete loading history should be further considered.

*Viscoelastic Behavior Considerations.* To simplify the mechanical analysis for viscoelastic materials, the selection of appropriate AFM probes and the environment (dry or liquid) should be considered to minimize the influence of adhesion on indentation experiments, due to complexity of corresponding phenomena. However, even if plastic deformation can be reduced by reducing the penetration depth, it is impossible to completely avoid viscoelastic contributions in the polymeric and biological materials in the vicinity of the glass transition. This contribution is especially important at the glass transition of the material, where material properties become highly deformation rate- and temperature-dependent. Several approaches to the measurements of time-dependent viscoelastic properties of polymeric materials that use AFM-based routines are discussed below.

The first approach is based on the direct measurements of polymer relaxation behavior in addition to the material compliance with traditional creep measurements.[48] A representative creep experiment for a viscoelastic material and corresponding deformational models are shown in Figure 4a.[47] During the creep experiment, at time $t_0$, the AFM tip is indented into the sample with force $F_0$ to a predetermined depth $\delta_0$. The force applied to the tip is then kept constant, and additional, slow time-dependent tip penetration of the surface is continuously monitored. At time $t'$, the force acting on the AFM tip is lifted and gradual recovery is monitored until equilibrium is reached at the final penetration depth, $\delta_f$. Because plastic deformation occurs during the creep experiments, initial material deformation is not fully recovered (residual strains) and $\delta_f \neq \delta_0$ (Figure 4a).[31]

Collected creep data is typically analyzed using two-element (spring (elastic) and dashpot (viscous)) Maxwell and Voigt models. However, these simple models cannot describe viscoelastic materials comprehensively because the Voigt model does not describe initial steep indentation and the Maxwell model does not provide the means for accounting for strain recovery.[31] To reduce the piezoelement creep over the large time period of loading and improve the signal-to-noise ratio, large indentations (hundreds of nanometers and even larger) are usually performed.[49] Unfortunately, these experimental conditions usually result in severe and unrecoverable plastic deformations. Therefore, a four-element model that can account for both the initial elastic response and the unrecoverable deformations must be selected for the analysis of such experiments (Figure 4a). Using this model, viscoelastic components can be calculated from the experimental data using equations[30]

$$\delta^{3/2} = \frac{3}{4}\frac{F_0}{\sqrt{R}}\left[\frac{(1-\upsilon^2)}{E_1} + \frac{(1-\upsilon^2)}{E_1}\left(1 - \mathrm{e}^{-tE_2/\eta_2(1-\upsilon^2)}\right) + \frac{1}{\eta_1}t\right] \tag{11}$$

$$\delta^{2} = \frac{\pi}{2}\frac{F_0}{\tan(\alpha)}\left[\frac{(1-\upsilon^2)}{E_1} + \frac{(1-\upsilon^2)}{E_1}\left(1 - \mathrm{e}^{-tE_2/\eta_2(1-\upsilon^2)}\right) + \frac{1}{\eta_1}t\right] \tag{12}$$

which are valid for spherical and conical tip shapes, respectively.

Creep data collection possesses several challenges when performed on the usual AFM devices. The initial steep increase in the surface deformation should be instantaneous, but it is in fact a ramp motion produced by the piezoelement. If the rate of this deformation is on the order of the relaxation time, then material relaxation will occur during the initial engagement and thus will not be completely accounted for. The time scale of this process is usually small in comparison to the full creep experiment time. However, because the experimental data is analyzed on the logarithmic time scale, the artificial deviations in calculated parameters can be significant.[47] Another challenge is related to maintaining a constant tip deflection during the loading portion of the creep curve. This can be achieved by the incorporation of a feedback algorithm that monitors the tip deflection and moves the piezoelement accordingly. Unfortunately, the piezoelement creep over large time scales contributes to significant and unaccounted for displacements that cannot be easily controlled.[50] In addition, long experimental times make the mapping of the viscoelastic properties over large surface areas with even modest spatial resolution impractical. Therefore, such measurements are usually conducted for a single point with an unknown topographical contributions and representation, which is especially critical for biological objects such as cells and multiphase materials with complex morphologies.[50]

Another commonly used method for viscoelastic measurements is called contact resonance force microscopy (CRFM) that involves dynamic phase-shift measurements.[51] A vibrating AFM tip is brought into mechanical contact with the surface, and the amplitude damping and phase shift of tip vibrations are recorded (Figure 4b). Next, the recorded values of the phase lag are analyzed by using a damped oscillator model for the tip−sample contact.[52] To calculate the mechanical properties of a material precisely, in addition to the tip−sample interactions a cantilever's flexural vibrational mode should be considered.[53] There are several mechanical models that describe damped cantilever vibrations; however, each of these models contains a substantial number of unknown parameters that are difficult to quantify.[52] Instead of a parametric model description, vibrational amplitudes are usually measured relative to the "free" cantilever vibration in CRFM experiments.[54]

In addition to the unknown tip−sample contact parameters, tip shapes are not measured directly but are determined indirectly from a reference material, which involves possible additional uncertainties.[27] CRFM is typically utilized for surface mapping with contrast caused by the difference in relative mechanical properties of the surface areas.[25] The mechanical properties of these different regions need to be relatively similar in order to apply this method. An additional challenge is the inability to probe at frequencies lower than the kilohertz to megahertz range as a result of the resonance properties of cantilevers, which are several orders of magnitude greater than any practical frequency range used for the traditional testing of polymeric or biological materials, thus direct comparison is compromised. Moreover, even the extrapolation of mechanical values obtained with these dynamic measurements to a practical frequency range (which can be theoretically conducted with master curve construction) can become very ambiguous as a result of very limited probing frequencies (usually limited by cantilever resonance modes). These measurements are performed at a single oscillation frequency with a fixed amplitude and generally provide only qualitative contrast information, which can be important for the mapping of composite surfaces. Therefore, a comparative mapping of relative surface properties with high spatial resolution can be considered to be an important applicability niche for this mode of operation. To obtain quantitative mechanical data, more complex approaches that involve force modulation and multifrequency measurements must be employed.[22,34]

Therefore, the goal of this Feature Article is to present a practical approach to the nanomechanical analysis of viscoelastic polymeric materials in glassy and rubbery states as well as in the immediate glass-transition region. The static SFS probing method presented in this work involves viscoelastic parameter extraction from FDCs collected at variable loading rates and different temperatures. We demonstrated that combining Sneddon's model with the common SLS model allows for the evaluation of storage and loss moduli and relaxation times over a wide range of temperatures and practical frequencies. It also allows more precise control over cantilever motion than dynamic measurements, reducing the number of unknown parameters of the model in a frequency range relevant to practical dynamic conditions. Additionally, in contrast to creep experiments, the present probing technique does not require a feedback loop and enables precise force control (outside of initial mechanical contact) because the time scale of the practical measurements is much faster than that of the piezoelement creep.

Finally, it is worth noting that we also verified that the traditional SFS probing conducted under the assumption of elastic deformation is applicable to the quantitative analysis of polymeric materials in glassy and rubbery states and is still adequate for qualitative analysis in the glass-transition range. This study can be considered as a natural development of the continuous efforts in our laboratory devoted to the micromechanical probing of various polymer materials such as polymer blends, block copolymers, elastomers, and hydrogels,[55−59] polymer and organic coatings such as polymer brushes, self-assembled monolayers, layer-by-layer films, porous polymers, and multilayered coatings,[60−65] and individual macromolecules, microcapsules, and biological materials,[66−68] as summarized in a recent book.[2] Below, we discuss the probing results, with the experimental details summarized in the Experimental Section.

## EXPERIMENTAL SECTION

**Materials.** For this study, we selected poly(*n*-butyl methacrylate) (PnBMA, weight-average molecular weight 337 000 g/mol, Sigma-Aldrich), which is a well-known amorphous polymeric material with a low glass-transition temperature. A saturated PnBMA solution (150 mg/mL) in toluene was cast in a glass Petri dish and held at 40 °C under vacuum for a week to remove residual solvent and to anneal this polymer film to a thickness of about 1 mm. According to the literature data, the $T_g$ of PnBMA is around 25 °C,[75,17] and thus all AFM measurements have been conducted at temperatures from 10 to 55 °C.

**AFM Measurements.** AFM and SFS measurements were performed on a Dimension Icon AFM instrument (Bruker) equipped with a Nanoscope V controller. Rectangular n-type Si cantilever probes (HQ:XSC11/Al BS) were obtained from MikroMasch. Spring constants of the cantilevers varied from 1.8 to 2.3 N/m and were measured via the thermal tuning method and selected to maximize the signal-to-noise ratio.[69,70] For each measurement, the actual tip shape was estimated independently by scanning 10−20 nm gold nanoparticles and performing tip-shape deconvolution.[71] Apex curvatures varied in the 10−50 nm range during the FDC collection procedure. Tip-shape measurements were repeated after probing the polymer materials if substantial changes in forces or irreproducible jumps had been observed (e.g., due to tip contaminations). The deflection sensitivity was determined by using a sapphire crystal.

Considering that liquid bridges between the AFM tip and the sample surface can produce significant forces to distort the information provided by the AFM,[72] all SFS measurements were conducted in ultrapure water (Millipore Corp) (18 MΩ·cm). This approach abates capillary bridge formation and reduces snap-to-contact forces, thus simplifying the data analysis dramatically. In addition, because ultrapure water is a bad solvent for PnBMA, artifacts in the FDCs due to surface swelling are avoided and the occurrence of surface contamination from ambient air is significantly reduced.

A small tip deflection of 4 nm was used in the experiments as verified to be the regime with no plastic deformation. Such measurements produced deflections with high signal-to-noise ratios while keeping indentations in the elastic regime and forces below 5−10 nN. For the consistency of SFS measurements, the displacement ramps for all experiments were kept constant at 150 nm. The cantilever *z* position was monitored via piezosensors for increased precision. Before and after the force measurements, AFM scans in light tapping mode were performed over the probing surface area to confirm the smoothness of the surface and the absence of nonrecovered plastic deformations after the measurements (indentation marks).

To visualize modulus variations over the full time and temperature scales, a set of force-volume measurements was performed at several probing frequencies. The frequency of the measurement was calculated as the reciprocal value of the time of a single FDC acquisition. Indentations at several different frequencies of 10, 5, 2.5, 1, 0.5, 0.25, and 0.125 Hz (with corresponding loading rates of 3000, 1500, 750, 300, 150, 75, and 37.5 nm/s for 150 nm ramps) were performed at different temperatures in the 10−55 °C range at 5 °C intervals. For each experiment, about 30 FDC curves were collected, averaged, and further analyzed. To account for possible piezoelement creep and AFM tip contamination, SFS measurements with deviations in the noncontact part of the curve greater than 25% of the maximum deflection observed after contact with the surface were excluded from further analysis. For each experiment, fewer than 20% of the individual measurements were excluded from further averaging. At each temperature and frequency, no significant deflections due to the liquid drag force were observed. (See the examples below.) Collected FDC curves were converted to loading curves in a conventional manner, and multiple runs have been averaged for further analysis.

For temperature variation experiments, samples were placed on a custom-made Peltier element/heating bath using silver conductive coating 18DB70X obtained from Electron Microscopy Sciences. Constant temperature was maintained during the experiment using a thermocouple feedback loop (ILX Lightwave LDT-5948 precision temperature controller) with temperature stability better than 0.01 °C.

**Evaluation of Mechanical Rates of Deformation.** To analyze acquired experimental data in the time−temperature domain, two approaches have been employed in the present study for the estimation of the time scale of the deformations. The first approach used the full time of one FDC acquisition cycle as the time scale of a single experiment. The second approach used only the portion of the curve when the tip and the sample were in the contact. For clarity, the term "apparent frequency" will be used to characterize the time scale in the first approach, and the term "loading frequency" will characterize the time scale related to the second approach. Because the change in the direction of the tip is controlled by the force threshold rather than by the actual indentation depth, the second approach gives a much more precise evaluation of the time of tip−sample interaction. As known, the contact portion of the FDC presents a varying fraction of the total curve acquisition time as the polymer softens during the polymer transition from the glassy state to the rubbery state. Therefore, two measurements performed at the same frequency below and above the glass transition will have different tip−sample interaction times and thus different deformation rates. This time difference presents a significant factor for the viscoelastic calculations and should be accounted for by considering actual deformation rates from FDC data.

Although not precise, the first approach of the time scale calculations gives the ability to compare FDC curves collected at different frequencies and does not require a precise knowledge of the contact fraction of the FDC. Therefore, it is widely utilized in the AFM community, especially in the case of simple elastic material behavior analysis, where only the contact portion of the FDC can be fitted for the elastic modulus calculation. Therefore, in the part of the present work where the fitting of the experimental data is performed under the assumption of simple elastic material behavior, the apparent frequency is used as the time scale of the experiment. For the calculations of the relaxation time ($\tau$) and loss and storage moduli ($E'$ and $E''$), the actual loading frequency that represents the reciprocal value of the calculated time of the tip−sample interaction should be employed.

**Measurements of Viscoelastic Polymer Behavior.** *FDC Collection with Low Impact.* In this study, FDC data was collected for PnBMA in a liquid cell at temperatures below, around, and above the nominal $T_g$ (about 25 °C).[17,75] Only the approaching curves were used for the viscoelastic properties' estimation to avoid large hysteresis in the course of retracting as a result of adhesive contributions and piezoelement creep. High capillary forces usually observed under ambient conditions for polymer surfaces (peak jump of 10−15 nN as demonstrated in Figure 5b) result in a high, uncontrolled initial surface deformation that compromises micromechanical probing, and thus SFS measurements in ambient air were excluded. To reduce the initial deformation due to strong capillary forces, all measurements in this study were performed in liquid, where modest snap-to jumps were observed (force variation below 20 pN, Figure 5a) that indeed facilitate fine SFS probing with high accuracy and minor uncertainties after initial mechanical contact. Indentation analysis performed in this study was based on the contact portion of the force−distance curve; therefore, determination of the contact point is a critical issue. Here we define the contact point as the point where the cantilever deflection deviates from the deflection baseline for more than a standard deviation of the baseline noise. For some setups, the presence of adhesive forces and a large amount of noise during the measurement can mask the contact point. In the case of simple elastic behavior, this can be accounted for by fitting only the well-defined part of the contact curve.[73] However, in the case of PnBMA the initial contact point was well-defined, as it can be judged from the behavior of the first derivative of deflection.[73]

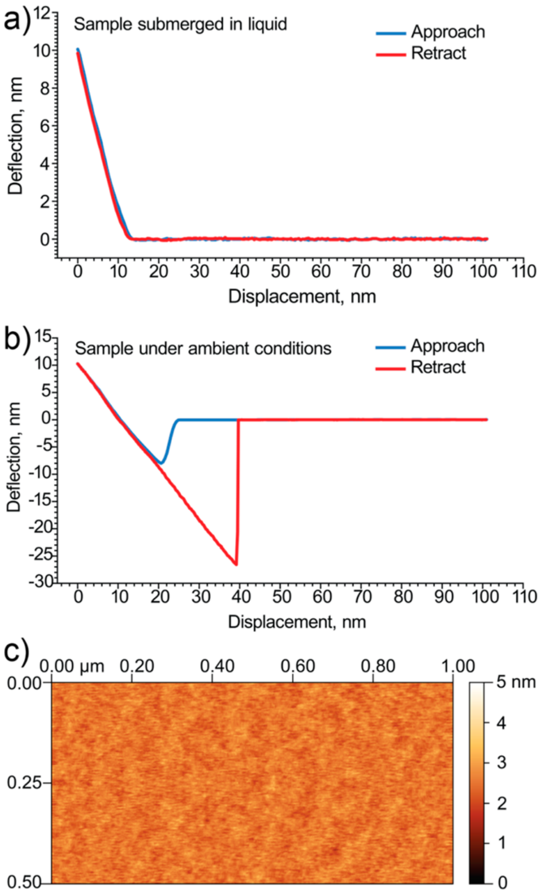

**Figure 5.** (a) Approaching and retracting curves for the in-liquid measurements of PnBMA at 25 °C and (b) the same measurements in an ambient humid environment. (c) AFM image of the PnBMA surface acquired in liquid at 25 °C.

High probing frequencies in this study were not affected by damping in liquid. The polymer surface was very smooth (microroughnesses of 0.3 nm within 500 nm × 500 nm surface areas), essentially eliminating data scattering related to topographical contributions at different probing locations (Figure 5c).

Examples of representative loading curves for the PnBMA surface collected at an intermediate apparent frequency of 2.5 Hz (a cantilever displacement rate of 750 nm/s), averaged over at least 20 different locations, at temperatures below, near, and above the glass transition (from 10 to 45 °C) are presented in Figure 6a. Overall, very modest indentations are exploited in this study, which are limited to 2−3 nm in the glassy state and 10−30 nm in the rubbery state to avoid plastic deformation and long relaxation processes (examples in Figure 7a). The scattering of the experimental data points is very modest as well. Apparently, the polymer surface becomes more complaint as the temperature rises above glass transition, as indicated by the doubling of the indentation depth up to 10 nm under the same mechanical load (Figure 6a). Additional heating well above the glass transition not only increases the compliance much further up but also completely changes the shape of the loading curve as a result of increasing viscous contributions with curvature of deflection versus displacement plot varying significantly in the 30−45 °C range (Figure 6a).

Several representative loading curves with different apparent frequencies for the fast (10 Hz or 3000 nm/s) measurements below $T_g$, slower measurements (1 Hz or 300 nm/s) at the onset of $T_g$, and slowest measurements (0.1 Hz or 30 nm/s) above $T_g$ are selected to show the combined role of the temperature and deformation rate

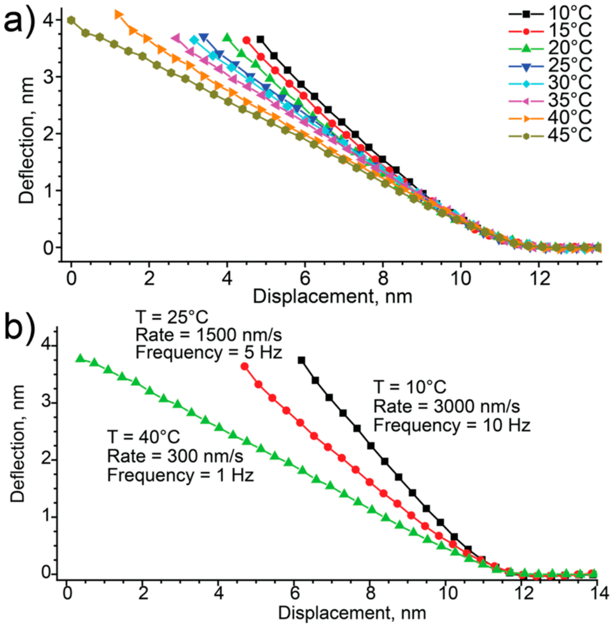

**Figure 6.** (a) Tip deflection−displacements curves for indentation experiments of PnBMA at different temperatures and at the same loading rate (750 nm/s). (b) Examples of representative force−distance curves at three characteristic temperatures: below, around, and above $T_g$.

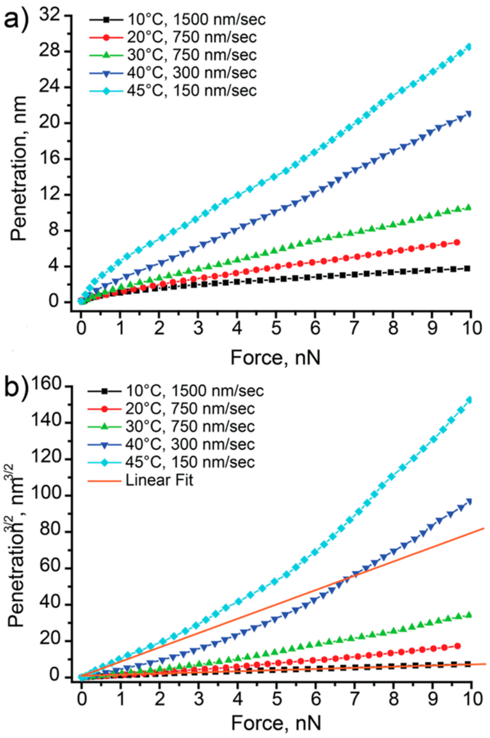

**Figure 7.** (a) Representative loading curves depicting the evolution of data with the temperature increase. (b) Corresponding (penetration)$^{3/2}$ data used for Sneddon's model and examples of the linear fit of the data in elastic and viscoelastic regimes (solid lines).

(Figure 6b). It is apparent that, for these coordinates, the rate variation results in the difference in the deformation behavior presented in Figure 6a being even more pronounced. This time−temperature complex behavior can be analyzed in terms of purely elastic and viscoelastic processes within the polymeric material, as will be discussed in detail below.

*Elastic Deformation.* Before going into the complex viscoelastic behavior discussion, the traditional simple elastic model based on Sneddon's analysis will be summarized below.[37] As was discussed above, assuming the AFM tip to be in the form of a rigid parabolic punch (Figure 2), the force applied to the elastic surface by the indenter is related to the elastic modulus, $E$, as

$$F = \frac{4}{3}\frac{a^3}{R}\frac{E}{1 - \upsilon^2} \tag{13}$$

where $a = (\delta R)^{1/2}$ is the radius of contact between the tip and the sample, $R = 2f$ is the radius of curvature of the apex of the parabolic tip, and $f$ is the focal distance (Figure 2). If the tip is described by the function $y = bx^2$, then this effective radius can be evaluated as $R = 1/2b$.

Knowledge of the force applied to the indenter as a function of penetration $F(\delta)$ during the loading experiment allows for the calculation of Young's modulus using a simple linear slope approximation:

$$E = \frac{3}{4}\frac{1 - \nu^2}{R^{1/2}}\frac{\mathrm{d}F}{\mathrm{d}(\delta^{3/2})} \tag{14}$$

It can be seen from eq 14 that, along with other independently determined experimental parameters, the simple elastic modulus ($E$) is simply a proportionality coefficient between the applied force and the elastic deformation of the sample.[17] It is important to note that unlike the Hertzian contact mechanics, the Sneddon's model describing a parabolic indenter shape, which is exploited here, does not have built-in limitation on very small deformation depths. This is not critical for current studies where the radius of contact is always well below the tip radius of curvature and minute adhesive forces for under-liquid probing virtually eliminate the initial jump-in event, which compromises further analysis.

*Modulus Variation with Time and Temperature Space: Simple Elastic Data Analysis.* To calculate the elastic modulus in Sneddon's approximation from the data collected in the form of FDCs, the penetration values should be considered (Figure 7a). Here, several representative FDC curves are shown to cover most of the range of observed material behavior from the glassy state at high loading rates and low temperatures to the rubbery state at low loading rates and high temperatures. Next, by using eq 13, the $\delta^{3/2}$ is plotted versus $F$ and linearly fitted using a zero intercept condition (solid line in Figure 7b). It can be seen that for SFS measurements at 10 and 20 °C (the glassy region for our polymer), the loading curves are perfectly described by a linear relationship as represented by eq 14 (coefficients of determination, $R^2$, are 0.995 and 0.993 for 10 and 20 °C, respectively). However, around 25 °C (close to the glass transition), the loading curves start to deviate strongly from simple linear behavior (solid line in Figure 7b, $R^2 = 0.95$ for 45 °C). This progressing deviation indicates that under these measurement conditions the polymer surface shows temperature- and loading-rate-dependent properties. Such deviations affect the evaluation of the elastic modulus accuracy, which drops dramatically at elevated temperatures and for nonlinear responses. While it is apparent that under these experimental conditions a simple Sneddon's model cannot describe the material behavior adequately, it does provide important insight into the overall material behavior, represents a practical elastic approximation, and thus is frequently utilized in current AFM measurements of presumably elastic solids even in the vicinity of the glass transition.[74]

Corresponding apparent elastic modulus values calculated from these linear fits (Figure 7b) for different temperatures and probing frequencies for our model polymer, PnBMA, are summarized in Figure 8a. Error bars in the plots, which are modest in different physical states, represent the calculated standard deviation from a set of about 20 individual SFS measurements. As is apparent from the analysis of this data set, at temperatures below 25 °C (below the nominal glass transition of the PnBMA material) the elastic modulus remains mostly unchanged at different loading rates and approaches an absolute value of around 1 GPa, which is a common value reported for PnBMA in the glassy state.[75] As expected, at elevated temperatures, a gradual decrease in the elastic modulus values from 1 GPa to 30−50 MPa for the highest temperatures (the rubbery state) and the slowest probing frequencies was observed (Figure 8a). These values are close to that reported in the literature for the rubbery state of PnBMA.[17]

The experimental data collected here can be further converted to the universal modulus-time−temperature relationship (the so-called master curve) by using the time−temperature superposition principle.[31] Indeed, the Williams−Landel−Ferry (WLF) equation provides the relationship between relaxation processes and temperature shifts at temperature $T$ and selected reference temperature $T_{\mathrm{ref}}$[76]

$$\log(a_T) = \frac{-C_1(T - T_{\mathrm{ref}})}{C_2 + (T - T_{\mathrm{ref}})} \tag{15}$$

where $a_T = f/f_{\mathrm{ref}}$ is the shift factor, $f$ is the current apparent frequency, $f_{\mathrm{ref}}$ is the reference apparent frequency, and $C_1$ and $C_2$ are constants for the material. If the reference temperature is selected to be the glass-transition temperature of the material, then universal constants $C_1 = 17.44$ and $C_2 = 51.6$ can be used for amorphous rubbery materials.[19] Using these universal constants and the glass transition as a reference temperature $T_{\mathrm{ref}} = 25$ °C for PnBMA, shift factors can be calculated and utilized to generate a universal master curve (Figure 8b). Such a universal master curve presents the values of the elastic moduli as projected over a much wider apparent frequency range ($10^{-3}$−$10^{4}$ Hz) and a wider temperature interval with the conversion between time and temperature scales presented on a double-horizontal axis in Figure 8b.

A similar analysis can be performed for the elastic modulus measurements grouped by apparent frequencies (Figure 9). At higher frequencies (higher loading rates), the temperature-dependent elastic

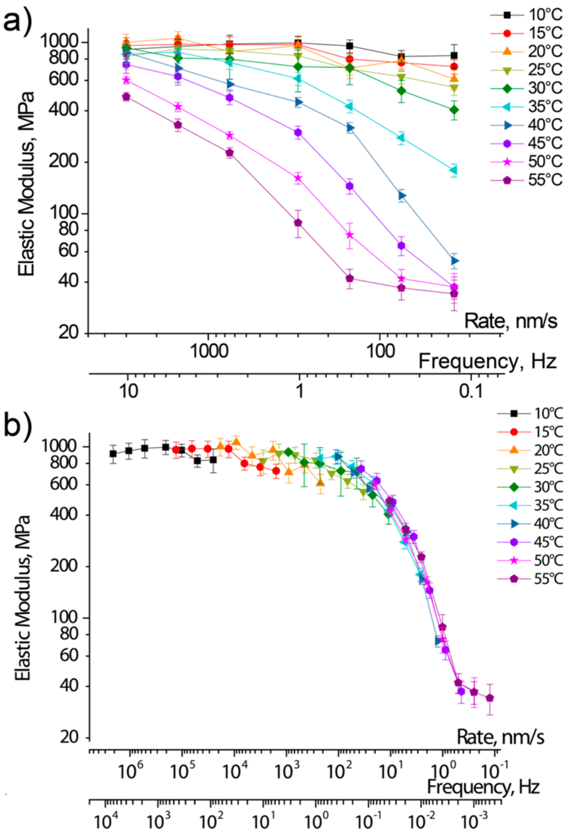

**Figure 8.** (a) Elastic moduli for PnBMA under different experimental conditions grouped by temperature. (b) Master curve constructed with the elastic Sneddon's model through the WLF equation at a reference temperature of 25 °C.

modulus is small over the full temperature range. In contrast, at lower frequencies, dramatic softening of the polymer surface can be observed at elevated temperatures (Figure 9a). This data can be further converted to the universal master curve as discussed above (Figure 9b). By shifting the frequency curves using the same universal constants $C_1$ and $C_2$ in relation to 1 Hz (300 nm/s), one can obtain a full master curve that fully relates time and temperature for the elastic modulus measurements of PnBMA (Figure 9b). The result of this approach is fully consistent with that generated above (Figure 8b and 9b).

A comparison of the master curves generated with two different conversion approaches shows that the temperature change is more versatile than the frequency variation in the sense that it allows for a broader range of the mechanical properties' variation to be projected. Such a high sensitivity of the measured modulus to the temperature in comparison to the loading rates arises from the power dependence of the shift factor on the temperature change (eq 15). This temperature sensitivity is important in the discussion of limitations of the time and temperature conversion procedures for the viscoelastic properties' analysis.

Overall, master curves generated here from SFS measurements under an assumption of elastic deformation closely resemble those expected from the literature data for polymer material with the glass transition at about 25 °C. The values of the elastic modulus in glassy (below 25 °C) and rubbery (above 50 °C) states are in good agreement with the known literature values.[17] However, the shape of the master curves in the temperature range around the glass-transition temperature with maximum mechanical energy dissipation (25−40 °C) is apparently compromised by the purely elastic deformation assumptions, and thus the polymer material behavior in this range requires a refined consideration by accounting for the dissipative behavior.

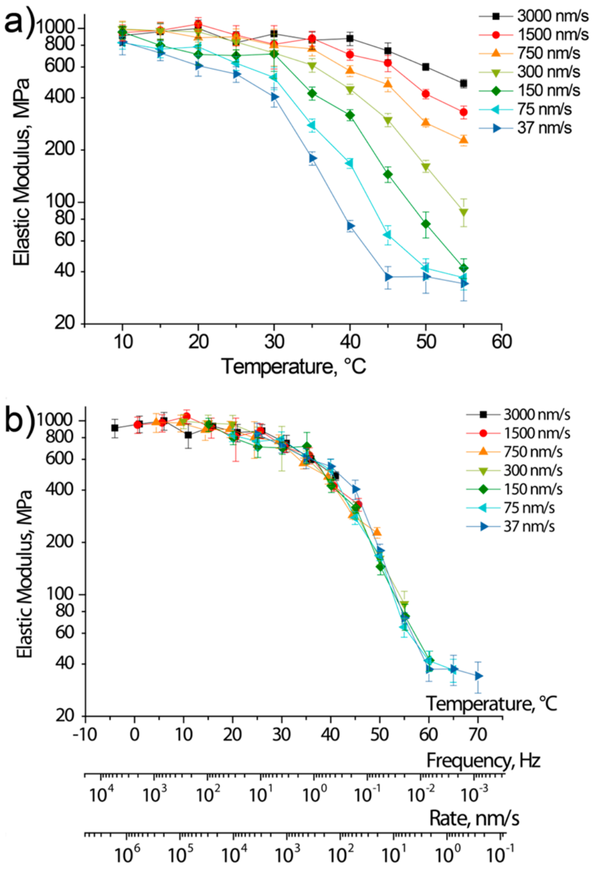

**Figure 9.** (a) Elastic moduli for the PnBMA under different experimental conditions grouped by frequency. (b) Master curve constructed with the elastic Sneddon's model through the WLF equation with the reference frequency at 1 Hz.

*Micromechanical Viscoelastic Analysis.* Here, we present the refined analysis of the experimental data in the glass-transition region with the viscoelastic SLS model, which deals with this limitation and allows for the evaluation of a full mechanical properties profile. This traditional SLS model is represented by a spring element attached in series to spring and dashpot elements connected in parallel (Figure 10a). The SLS model is well known to represent the time-dependent behavior of viscoelastic materials accurately without residual strains and has already been applied to SFS analysis.[77,78]

We do not use a more complex four-element model because we concentrate on the region of the stress−deformation curve where no unrecoverable deformations are present. In contrast to the SLS model, the more complex four-element model will never equilibrate because of the presence of plastic flow that is next to impossible to account for (Figure 4a). For higher loads, which lead to unrecoverable deformation (plastic deformation), an additional viscous element should be added to describe the system behavior adequately. Such a change, however, significantly complicates the data analysis and makes overall data processing extremely cumbersome, ambiguous, and unstable.[30]

The traditional SLS model exhibits very well known time-dependent behavior, which can be represented by the time-dependent modulus variation (compliances, $J \approx {}^{1}/_{E}$, are presented in Figure 10b). This general schematic shows that after instantaneous step loading the SLS system will immediately respond as a perfectly elastic material with an instantaneous modulus, $E_0$. Next, because of the presence of the dashpot with the dynamic viscosity, $\eta$, a second spring will undertake the load partially and gradually over time, until eventually the SLS system will equilibrate with the initial load distributed between two springs exhibiting the effective infinite modulus, $E_\infty$ (Figure 10b). In the SLS viscoelastic material, at any given time $t$ the

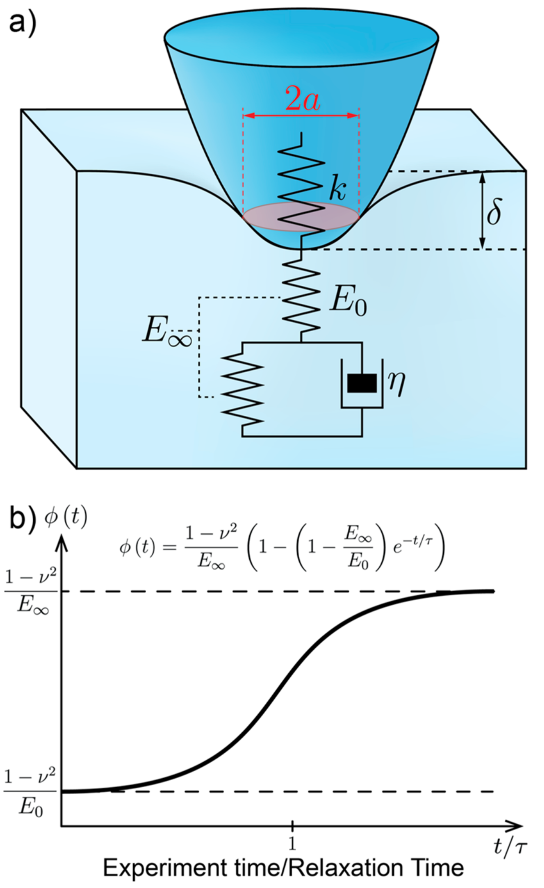

**Figure 10.** (a) Sneddon's model applied to the case of viscoelastic SLS material. (b) Creep-compliance function for SLS material.

coefficient of proportionality between the stress and the strain can be described by the creep-compliance function, $\varphi(t)$, in accordance with the relationship[79]

$$\varphi(t) = \frac{1-\upsilon^2}{E_\infty}\left(1 - \left(1 - \frac{E_\infty}{E_0}\right)\mathrm{e}^{-t/\tau}\right) \tag{16}$$

where $\tau = [(E_0 - E_\infty)/(E_0 E_\infty)]\eta$ is the relaxation time of the viscoelastic material. Thus, the creep-compliance function, $\varphi(t)$, is the representation of a single rate-dependent elastic modulus of the material (Figure 10b).

To describe the loading behavior for an SLS material during an indentation experiment, Johnson[79] suggested the application of the viscoelastic correspondence principle to Sneddon's elastic model. He has derived the modified relationship for the variation of the contact area $a$ of the axisymmetric indenter represented by a complex function instead of eq 1 for purely elastic deformation[79]

$$a^3(t) = \frac{3R}{4}\int_0^t \varphi(t-t')\frac{\mathrm{d}}{\mathrm{d}t'}F(t')\,\mathrm{d}t' \tag{17}$$

and the penetration depth to be calculated as

$$\delta^{3/2}(t) = \frac{3}{4\sqrt{R}}\int_0^t \varphi(t-t')\frac{\mathrm{d}}{\mathrm{d}t'}F(t')\,\mathrm{d}t' \tag{18}$$

which replaces the simple elastic relationship (eq 14).

It is important to note that in contrast to the case of a simple linear elastic material, eq 18 for the SLS viscoelastic material represents the loading-rate-dependent relationship. As suggested by Johnson,[79] in the case of a constant loading rate $U = \mathrm{d}/\mathrm{d}t\ F(t)$ (common mode of operation during the SFS data collection procedure), eq 18 can be simplified to

$$\delta^{3/2}(t) = \frac{3UT}{4\sqrt{R}}\frac{1-\upsilon^2}{E_\infty}\left(\frac{t}{\tau} - \left(1 - \frac{E_\infty}{E_0}\right)(1 - \mathrm{e}^{-t/\tau})\right) \tag{19}$$

The three unknown parameters $E_0$, $E_\infty$, and $\tau$ in eq 19 can be found by fitting the experimental time-dependent loading data as well as independent measurements of $E_\infty$ and $E_0$ under limiting conditions as discussed below. In all of the following calculations, a time scale was derived from the loading frequency as discussed in the Experimental Section. It is worth noting that this analysis must be used only on the approaching part of the indentation curve because it accounts only for the compressive load.[79]

For extremely long and short experimental times, the creep compliance function presents two limiting cases of the material behavior represented by two different values of elastic moduli (Figure 10b). Johnson's model inherits this feature; therefore, these special cases can be explored for independent measurements of the limiting elastic moduli values, $E_0$ and $E_\infty$. To analyze these extreme cases, it is useful to plot the penetration in dimensionless coordinates as normalized to penetration at a selected reference time (Figure 11a).

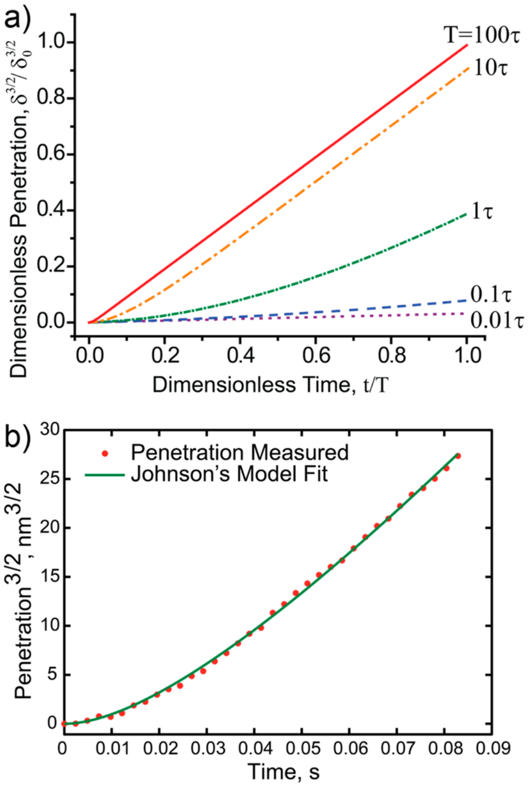

**Figure 11.** (a) Theoretical penetration curves for SLS materials with different relaxation times plotted in dimensionless coordinates. (b) Example of fitting the actual experimental data with Johnson's model.

Such an aproach allows for the reduction of the difference in deformation of glassy and rubbery states, therefore facilitating the observation of overall model behavior in a broad range of loading rates and temperatures.

Following the approach introduced by Johnson,[79] the normalized penetration is plotted against dimensionless time for several values of the reduced measurement time, $T$ (Figure 11a). In this plot, the $x$ axis is normalized by the loading time $T$ (time of tip–sample contact during the approach part of FDC). The $y$ axis is normalized by the penetration $\delta_0$ calculated under the assumption of infinite relaxation time as if the material would have perfectly elastic behavior with an infinite elastic modulus $E_\infty$. With such normalization of the $y$ axis, the relative penetration at time $t/T$ will vary from $E_\infty/E_0$ to 1 depending on the rate of the experiment. Using such an approach, one can examine the relaxation behavior on different time scales relative to relaxation time $\tau$ without a knowledge of the absolute values of $\tau$. However, one should still make assumptions about the ratio $E_\infty/E_0$ of elastic properties of the model in extreme cases of short and long measurement times. As an example here, we use the values $E_0$ = 958 MPa and $E_\infty$ = 30 MPa obtained experimentally for PnBMA at extremely high and low probing frequencies.

The two limiting cases where the relative penetration changes linearly with time stand out immediately from this reconstruction (Figure 11a). Under short loading times, $t \ll \tau$, eq 19 is reduced to the simple elastic relationship (eq 14) with $E = E_0$. However, at very slow measurements for the points where $t \gg \tau$, the behavior is again elastic with $E = E_\infty$. For the second case, however, it is important to note that linearity does not hold for a limited probing time range where $t \approx \tau$, as can be seen in Figure 11a for the case of $T = 10 - 100\tau$. Therefore, under these conditions, one should use the latest stages of the loading curve for the linear fitting in order to analyze the quasi-elastic behavior. For the relaxation times in between these two extreme cases, nonlinear behavior is observed with continuous slope variation during the loading cycle (Figure 11a).

An important practical observation can also be made from the dynamic penetration reconstruction presented in Figure 11a. Because in the extreme cases of slow and fast measurements described above, the SLS model follows the standard elastic behavior and parameters $E_\infty$ and $E_0$ can be estimated from the experimental measurements under these very different loading time conditions using eq 14. The SLS model assumes no variation in the infinite and instantaneous moduli with the changes in the time scale of the measurement. Therefore, limiting parameters $E_\infty$ and $E_0$ can be used for the calculations outside of the linear deformation regions. According to this consideration, values of the relaxation time can be found by fitting the experimental penetration data using eq 19 with known values of $E_\infty$ and $E_0$ with $\tau$ as the single fitting parameter.

Taking into account the aforementioned behavior of the SLS model, we adapted the following analysis procedure in this study and can recommend it as a standard procedure. First, the values of $E_0$ and $E_\infty$ must be experimentally found by fitting the loading data for the limiting regions of the perfect elastic behavior at low temperatures and high frequencies for $E_0$ and, inversely, at high temperatures and low frequencies for $E_\infty$. The loading curve was assumed to be linear if the standard error of the linear fit was less than 5%.[80] Notably larger deformational stages were used for $E_\infty$ calculations to meet the $t \gg \tau$ condition (e.g., the curve collected at 45 °C, Figure 7b). Both values ($E_0$ = 958 MPa and $E_\infty$ = 30 MPa) corresponded well to limiting values derived from the master curve (Figure 8b) and are indeed close to that reported for PnBMA material in glassy and rubbery states.[17] Thus, these values were used for further analysis in the viscoelastic regime.

Before going into the analysis of the deformation in the viscoelastic region, we should discuss the load application. The piezoelement does not apply pressure to the tip−sample contact region directly. Instead, a base of the compliant cantilever is displaced so that the actual applied force depends on the force balance between the deflected cantilever and the displaced sample surface. In the case of fast loading in the elastic regime, the equilibrium between the tip and the sample is instantaneous; therefore, the tip of the cantilever moves with the same rate as its base. However, in the viscoelastic regime, the presence of a dashpot in the system does not allow for the instantaneous deformation of the material, resulting in a lag between the motion of the base of the cantilever and its tip.

Examples of this behavior are presented in Figure 12 as actual time-dependent deflection data sets for the extreme cases of fast and slow measurements (apparent frequencies 10 and 0.1 Hz) and two temperatures (10 and 45 °C). It is apparent from these examples that at 10 °C the motion of the cantilever is linear with time and the approach and retract portions of the curve are symmetrical. When PnBMA is heated to 45 °C, the viscoelastic behavior becomes prominent as the loading becomes nonlinear and asymmetric against the point of maximum deflection, which is especially notable for the 0.1 Hz case (Figure 12).

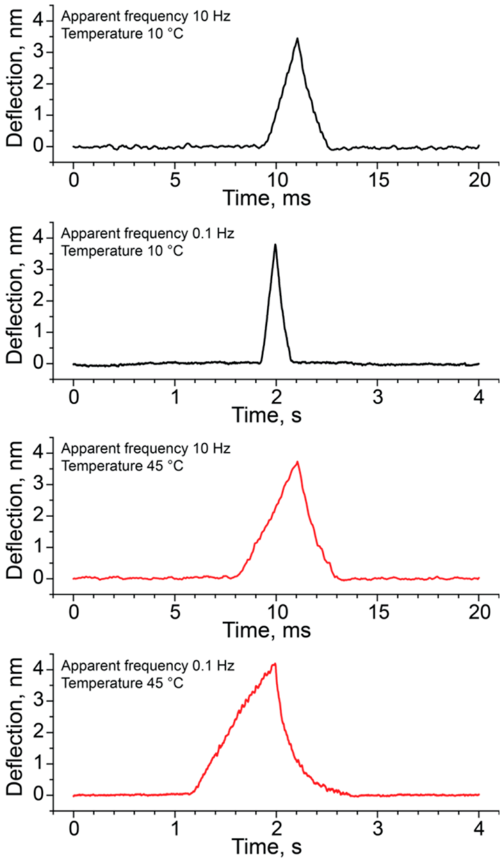

**Figure 12.** Examples of the deflection vs time data collected for PnBMA at 10 and 45 °C with apparent frequencies of 10 and 0.1 Hz.

Therefore, although the base of the piezoelement extends at a constant rate in all experiments, eq 19 derived for a constant loading rate is limited to fitting data collected at high rates and low temperatures. However, because $E_0$ and $E_\infty$ were determined from the elastic conditions, the relaxation time $\tau$ is the only unknown parameter and eq 18 can be used to fit the loading data with $\mathrm{d}F(t')/\mathrm{d}t$ calculated from the smoothened deflection data. Fitting was also done with eq 19 calculated under the assumption of a constant loading rate. Experimental data were analyzed using unconstrained nonlinear optimization with MATLAB software.

It is worth noting that a comparison of the fitting errors and calculated relaxation times showed less than a 5% difference between analytical (linear) and numerical (actual) forms of the Johnson model in cases of the highest nonlinearity of the loading rates (around 45 °C) (Figure 12). However, because the computational time for fitting with eq 18 is greater than 10-fold more time-consuming, all calculations were performed under the constant loading rate assumption (eq 19). An example of such a fitting is presented in Figure 11b for the indentation measurements performed at 40 °C at a 2.5 Hz apparent frequency (750 nm/s loading rate). In this particular case, the relaxation time was found to be $\tau$ = 0.7s.

Similar SLS analysis was performed at different temperatures and resulted in the evaluation of the temperature dependency of the relaxation times at several different temperatures above $T_g$ (within 35−55 °C) (Figure 13). For temperatures below 35 °C, loading curves showed very small deviations from the linear elastic behavior; therefore, the relaxation time estimation could not be performed properly because of the relaxation times being much longer than the measurement times. Assuming Arrhenius-type behavior in this temperature range and plotting ln($\tau$) versus inverse temperature, 1/$T$, we can estimate the apparent activation energy associated with relaxation processes involved in the material deformation from the slope of the experimental data (Figure 13a).[31] In this way, the

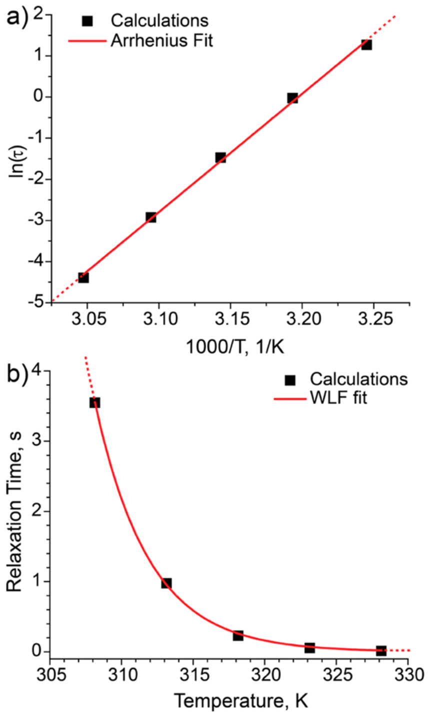

**Figure 13.** (a) Arrhenius plot for the temperature dependence of relaxation time and its linear fit. (b) Absolute values of relaxation time calculated through Johnson's viscoelastic model and the WLF equation fit of the relaxation time data.

apparent activation energy was found to be around 230 kJ/mol, which is close to the values found in the literature for the relaxation processes related to the unfreezing of the segmental mobility of macromolecular chains of PnBMA during the glass transition.[81,82]

Next, the temperature variation of the relaxation time for a wider temperature range was evaluated by using the extrapolation from the WLF equation. In this approach, the dependence of the relaxation time on temperature is analyzed by employing a WLF-type relationship in the form[76]

$$\tau = \tau_{\mathrm{ref}} 10^{-C_1(T-T_{\mathrm{ref}})/C_2+(T-T_{\mathrm{ref}})} \qquad (20)$$

The corresponding fitting of the experimental data resulted in a wide spectrum of relaxation times (Figure 13b). Fast relaxation times of about 10 ms were evaluated in the rubbery state at the highest temperatures probed here (around 55 °C). However, the relaxation process slows dramatically to about 4 s at lower temperatures close to the glass transition. It is important to note that these values of the relaxation time are close to the independent literature values obtained by photon correlation studies for the same polymer in a similar temperature range.[82]

Finally, by using the values of relaxation times measured above, it is possible to characterize the mechanical properties of PnBMA fully over a wide temperature range by using the classical relationships derived from the SLS model for viscoelastic materials.[31] In this model (see discussion above and Figure 10), the values of the storage modulus $E'$, loss modulus $E''$, and loss tangent $E''/E'$ can be calculated by using the relaxation times $\tau$ and limiting values $E_0$ and $E_\infty$, which have been measured independently[83]

$$E' = E_\infty \frac{1 + \omega^2\tau^2(E_\infty/E_0)}{1 + \omega^2\tau^2(E_\infty/E_0)^2} \qquad (21)$$

$$E'' = E_\infty \frac{\omega\tau(1 - (E_\infty/E_0))}{1 + \omega^2\tau^2(E_\infty/E_0)^2} \qquad (22)$$

where $\omega$ is the angular frequency and can be calculated from the loading temporal frequency $f$ through the relation $\omega = 2\pi f$. It is important to note the difference between the tip−sample interaction time and the apparent measurement time as discussed in the Experimental Section.

The final evaluation of the viscoelastic mechanical properties from the SLS viscoelastic model by using eqs 21 and 22 for PnBMA is presented in Figure 14. Relaxation times outside the 35−55 °C region were extrapolated from the experimental data using eq 20. For the following calculations, the reference tip−sample interaction time was selected to correspond to a standard loading frequency of 1 Hz. The temperature variations of $E'$, $E''$, and $E''/E'$ in the temperature range of 10−70 °C derived from this analysis and experimental data show characteristic features of dynamic measurements of polymeric materials with characteristic features of a glass transition (Figure 14).[19] Because the relaxation values were extrapolated using the 35−55 °C temperature region, $\beta$ relaxation below $T_g$ is not included in the reconstructed plot and thus the loss modulus has a symmetrical shape and reaches zero from both sides.

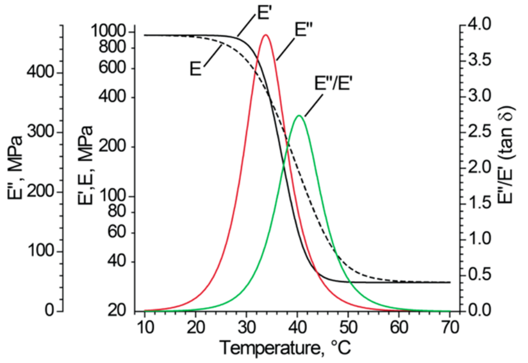

**Figure 14.** Storage ($E'$) and loss ($E''$) moduli and tan $\delta$ plots for PnBMA under the SLS behavior assumption (solid lines). Master curve for the apparent elastic modulus for PnBMA calculated from the elastic Sneddon's model fit of the penetration data acquired from the SLS model (dashed line).

It is important to note the difference in this plot and bulk dynamic mechanical analysis (DMA) measurements.[84] During conventional DMA measurements, the presence of additional group relaxation in the glassy state causes the left shoulder of the loss modulus to increase its maximum value by 5%. The storage modulus shows the transition region at 25−50 °C with a dramatic drop in the modulus value during the transition from the glassy state to the elastic rubbery state. An onset of the sharp modulus change is around 27 °C, which corresponds to the glass transition of PnBMA.[75,17]

The maximum value of the loss tangent, calculated from the SLS model, is shifted to an elevated temperature (around 40 °C), which is consistent with the common dynamic mechanical measurement trends for polymeric materials in the viscoelastic regime.[31] It is important to point out that eqs 21 and 22 exhibit a dependence on the measurement rate $\omega$; therefore, plots of $E'$, $E''$, and $E''/E'$ will be shifted along the temperature axis if different loading frequencies other that 1 Hz are selected. Another important feature that should be noted here is the fact that eq 20 is not valid below $T_g$, where a special form of the Arrhenius dependence should be used;[31] therefore, the relaxation times cannot be accurately estimated from the proposed extrapolation in this temperature range. However, glassy materials show purely elastic behavior under small deformations, and thus the mechanical response under these conditions can be described by the elastic model.

It is useful to compare the results for the storage modulus variation reconstructed in Figure 14 to the linear penetration data fitting (elastic approximation) to evaluate the applicability of the simple Sneddon's model to the viscoelastic regime. To compare two sets of evaluations, the following procedure was used. Penetration versus force data were reconstructed for 1 Hz measurements in the 10−70 °C temperature range using measured relaxation times $\tau$ along with the independently measured limiting cases of modulus values $E_0$ and $E_\infty$ using eq 19.

Next, these curves were fitted using the traditional Sneddon approach to obtain an "integrated" elastic modulus value, $E$, for each temperature under the elastic approximation (Figure 14, dashed line). Reconstructed penetration versus force data were used instead of the experimental data in order to compare only the mathematical models and neglect the possible contribution of the measurement noise introduced by the SFS measurements.

From the temperature variations for the elastic modulus values restored under the purely elastic conditions assumption, we can conclude that the Sneddon elastic model accurately predicts the behavior of storage modulus $E'$ in both glassy and rubbery regions with deviations of less than 5% (Figure 14). However, in the glass-transition region of the polymer material (from 25 to 55 °C) the differences between $E'$ values calculated with the viscoelastic model and that derived from purely elastic model can be substantial. For example, at 10 °C below the glass-transition temperature, the apparent elastic modulus is 20% below the true storage modulus. Moreover, the most pronounced difference (more than 3-fold) is observed within a narrow temperature range (around 43 °C), with the highest loss of mechanical energy occurring where the loss tangent $E''/E'$ reaches its maximum value (Figure 14). Such large differences are caused by the fundamental fact that in this highly viscoelastic region the $\delta^{3/2}$ versus $F$ plot is very nonlinear and cannot even be remotely approximated with a linear relationship (Figure 7). Such a large deviation renders simple elastic analysis incorrect and irrelevant by overestimating the true storage modulus manifold by not considering sharply increased contributions from the dominating loss modulus. In this region of active unfreezing of segmental chain motion and steep increases in mechanical energy dissipation, the traditional Sneddon-based elastic probing measures only the initial fast deformational response, and the time-dependent resistance is essentually interpreted as a rising elastic modulus rather than an increasing contribution of the loss modulus component.

Again, after a full transition to the elastic rubbery state at elevated temperatures (above 50 °C for PnBMA), the apparent values of the elastic modulus evaluated with the purely elastic model become close to the true value as a result of the dramatic reduction of the loss modulus and again return to the elastic deformation regime (but with a greater deformation) (Figure 14). Overall, this analysis shows that outside of a temperature region that can be defined as $T_g \pm 15$ °C, the Sneddon elastic model can be applied for an accurate quantitative determination of the true elastic modulus with a high accuracy (within ±10−15%). However, in close proximity to $T_g$ (an approximately 30 °C transition range for this material), the apparent value of the elastic modulus derived under the assumption of elastic deformation deviates strongly from the true storage modulus as a result of dominating energy dissipation that is unaccounted for by the elastic model. In this temperature range, the SLS viscoelastic model must be used in conjunction with the Johnson−Sneddon treatment to restore the true values of both storage and loss moduli at low deformational rates relevant to practical applications of polymeric materials.

## ■ CONCLUSIONS

We summarized the methods of SFS probing of nanomechanical properties of polymeric and biological materials with time-dependent behavior. We discussed the traditional application of the shape-dependent Sneddon model for different experimental conditions and the limitations of the common indentation methods used for hard materials in studies of soft matter. More importantly, we have evaluated several current approaches for probing the viscoelastic properties using special loading methods such as creep and dynamic loading. We suggested that creep measurements can be used to characterize the mechanical properties of the viscoelastic materials quantitatively but require high precision control over the piezoelement displacement, relatively long time scales of the measurement, and a constant deflection retention feedback loop. Dynamic loading methods with high scan rates are not subjected by the piezoelement creep and thus can be readily applied to mapping of differential surface mechanical properties including storage and loss properties with high spatial resolution. However, these methods require a complete theoretical description of the tip motion and therefore are the best fit to high-rate qualitative characterization and contrast imaging of multiphase materials. They have limited use for the measurement of very soft materials with small differences in elastic response.

Finally, we have elaborated an example of the experimental and analysis routine for the evaluation of the viscoelastic properties of a model polymeric material using static force−distance data collected at a variety of loading rates and different temperatures across glassy and rubbery regions by using a combined Johnson−Sneddon model for the quantitative analysis of the time-dependent polymer material properties. Critical steps in obtaining unambiguous temperature dependencies of loss and storage moduli are a tip with a well-characterized parabolic shape, a liquid environment with reduced capillary forces, and very minute indentations to ensure the absence of plastic deformation.

The analysis of the experimental data with appropriate models (Sneddon's model for elastic regions (glassy and rubbery) and SLS-based Johnson's model for the viscoelastic region) allowed for the restoration of the universal master curve for the polymer materials under investigation with full temperature−time-dependent behavior restored for the storage modulus, loss modulus, loss tangent, relaxation times, and activation energies. The standard elastic Sneddon's model generates adequate modulus values below and above the glass transition but can significantly underestimate the actual modulus values within the glass-transition region ($T_g \pm 15$ °C), with major deviations occurring at the peak of the loss tangent. A comparison of the master curves obtained with the viscoelastic Johnson−Sneddon model from the experimental data showed that the standard viscoelastic SLS model adequately describes the viscoelastic materials' behavior in the temperature region of the glass transition.

## ■ AUTHOR INFORMATION

### Corresponding Author

*E-mail: vladimir@mse.gatech.edu.

### Notes

The authors declare no competing financial interest.

### Biographies

Marius Chyasnavichyus earned his B.S. degree in physics from the Russian State University of Aviation Technology and his Ph.D. degree from the School of Materials Science and Engineering at Clemson University working on grafted fluorescent polymer films. Currently he works as a postdoctoral researcher in the Surface Engineering and Molecular Assemblies Laboratory at Georgia Institute of Technology. He conducts experimental and theoretical research on the nanomechanical properties of soft matter using AFM techniques.

Seth Young earned his B.S. with high honors from the School of Materials Science and Engineering at Georgia Institute of Technology. In 2010, he began working towards his Ph.D. under the supervision of Professor Tsukruk. His current research focuses on determining the viscoelastic nanomechanical properties of strain-actuated slit sensors in the exoskeleton of wandering spiders using AFM as the primary characterization technique. Additionally, he has assisted with characterizing other biomaterials using AFM including silk, recombinant silk proteins, and layered hydrogels.

Vladimir V. Tsukruk is a professor in the School of Materials Science and Engineering, Georgia Institute of Technology, and is a member of the GT Bioengineering Program, Institute of Bioengineering and Bioscience, and the Center for Organic Photonics and Electronics. Tsukruk is a founding co-director of the Air Force BIONIC Center of Excellence and a founding director of the Microanalysis Center. His research laboratory, SEMA (Surface Engineering and Molecular Assemblies, http://polysurf.mse.gatech.edu/) conducts sustained research in the fields of polymeric nanocomposites, organic–inorganic surfaces and interfaces, directed assembly and self-assembly, natural and synthetic biopolymers, biological receptors, and responsive polymers. He has coauthored around 370 refereed articles as well as 5 books, which have been cited about 12 000 times, has organized 10 professional conferences, and has trained about 60 students and postdoctoral researchers. He received his M.S. degree in physics from the National University of Ukraine and Ph.D. and D.Sc. degrees in chemistry and polymer science from the National Academy of Sciences of Ukraine and carried out his postdoctoral research at U. Marburg, TU Darmstadt, and U. Akron. His recent rewards have been the Humboldt Research Award (2009) and the NSF Special Creativity Award (2006), among others, and he was elected as an APS Fellow in 2010 and an MRS Fellow in 2011. His recent book, *Scanning Probe Microscopy of Soft Matter: Fundamentals and Practices* (Wiley, 2012), is a comprehensive textbook on SPM applications to synthetic and biological materials. He serves on the editorial advisory boards of professional journals *Polymer*, *Langmuir*, *ACS Applied Materials & Interfaces*, and *Advances in Materials Science and Engineering.*

## ■ ACKNOWLEDGMENTS

Financial support from the National Science Foundation, Division of Materials Research under awards DMR-1209332 and DMR-1002810, and the Air Force Office of Scientific Research through the FA9550-11-1-0233 project is gratefully acknowledged. We thank Dr. V. Gorbunov (Bruker) for reading the manuscript and making useful suggestions.

## ■ REFERENCES

(1) Swallowe, G. M. *Mechanical Properties and Testing of Polymers: An A–Z Reference*; Kluwer Academic: Dordrecht, The Netherlands, 1999.

(2) Tsukruk, V. V.; Singamaneni, S. *Scanning Probe Microscopy of Soft Matter Fundamentals and Practices*; Wiley-VCH: Weinheim, Germany, 2012.

(3) Domke, J.; Radmacher, M. Measuring the elastic properties of thin polymer films with the atomic force microscope. *Langmuir* **1998**, *14*, 3320–3325.

(4) Johnson, K. L. *Contact Mechanics*; Cambridge University Press: Cambridge, U.K., 1987.

(5) Samori, P.; Cicoira, F. *STM and AFM Studies on (Bio)Molecular Systems: Unravelling the Nanoworld*; Springer: Berlin, 2008.

(6) Tsukruk, V. V.; Wahl, K. *Microstructure and Microtribology of Polymer Surfaces*; American Chemical Society: Washington, DC, 2000.

(7) Magonov, S.; Whangbo, M.-H. *Surface Analysis with STM and AFM: Experimental and Theoretical Aspects of Image Analysis*; VCH: New York, 1996.

(8) Ratner, B. D; Tsukruk, V. V. *Scanning Probe Microscopy of Polymers*; American Chemical Society: Washington, DC, 1998.

(9) Zhang, W.; Zhang, X. Single molecule mechanochemistry of macromolecules. *Prog. Polym. Sci.* **2003**, *28*, 1271–1295.

(10) Kuhner, F.; Gaub, E. H. Modelling cantilever-based force spectroscopy with polymers. *Polymer* **2006**, *47*, 2555–2563.

(11) Shulha, H.; Wong, C.; Kaplan, D. L.; Tsukruk, V. V. Unfolding the multi-length scale domain structure of silk fibroin protein. *Polymer* **2006**, *47*, 5821–5830.

(12) Binnig, G.; Quate, C. F.; Gerber, C. Atomic force microscope. *Phys. Rev. Lett.* **1986**, *56*, 930–933.

(13) Derjaguin, B. V.; Muller, V. M.; Toporov, Y. P. Effect of contact deformations on the adhesion of particles. *J. Colloid Interface Sci.* **1975**, *53*, 314–326.

(14) Johnson, K. L.; Kendall, K.; Roberts, A. D. Surface energy and the contact of elastic solids. *Proc. R. Soc. A* **1971**, *324*, 301–313.

(15) Maugis, D. Adhesion of spheres: The JKR-DMT transition using a Dugdale model. *J. Colloid Interface Sci.* **1992**, *150*, 243–269.

(16) Oliver, W. C.; Pharr, G. M. An improved technique for determining hardness and elastic modulus using load and displacement sensing indentation experiments. *J. Mater. Res.* **1992**, *7*, 1564–1583.

(17) Cappella, B.; Kaliappan, S. K.; Sturm, H. Using AFM force–distance curves to study the glass-to-rubber transition of amorphous polymers and their elastic–plastic properties as a function of temperature. *Macromolecules* **2005**, *38*, 1874–1881.

(18) Roylance, D. *Engineering Viscoelasticity*; MIT: Cambridge, MA, 2001.

(19) Sperling, L. H. *Introduction to Physical Polymer Science*; Wiley: Hoboken, NJ, 2006.

(20) Cappella, B.; Kaliappan, S. K. Determination of thermomechanical properties of a model polymer blend. *Macromolecules* **2006**, *39*, 9243−9252.

(21) Yang, G.; Rao, N.; Yin, Z.; Zhu, D.-M. Probing the viscoelastic response of glassy polymer films using atomic force microscopy. *J. Colloid Interface Sci.* **2006**, *297*, 104−111.

(22) Igarashi, T.; Fujinami, S.; Nishi, T.; Asao, N.; Nakajima, K. Nanorheological mapping of rubbers by atomic force microscopy. *Macromolecules* **2013**, *46*, 1916−1922.

(23) Garcia, R.; Gomez, C. J.; Martinez, N. F.; Patil, S.; Dietz, C.; Magerle, R. Identification of nanoscale dissipation processes by dynamic atomic force microscopy. *Phys. Rev. Lett.* **2006**, *97*, 016103−016104.

(24) Wang, D.; Liang, X.-B.; Liu, Y.-H.; Fujinami, S.; Nishi, T.; Nakajima, K. Characterization of surface viscoelasticity and energy dissipation in a polymer film by atomic force microscopy. *Macromolecules* **2011**, *44*, 8693−8697.

(25) Killgore, J. P.; Yablon, D. G.; Tsou, A. H.; Gannepalli, A.; Yuya, P. A.; Turner, J. A.; Proksch, R.; Hurley, D. C. Viscoelastic property mapping with contact resonance force microscopy. *Langmuir* **2011**, *27*, 13983−13987.

(26) Kovalev, A.; Shulha, H.; Lemieux, M.; Myshkin, N.; Tsukruk, V. V. Nanomechanical probing of layered nanoscale polymer films with atomic force microscopy. *J. Mater. Res.* **2004**, *19*, 716−728.

(27) Yuya, P. A.; Hurley, D. C.; Turner, J. A. Contact-resonance atomic force microscopy for viscoelasticity. *J. Appl. Phys.* **2008**, *104*, 074916−7.

(28) Yuya, P. A.; Hurley, D. C.; Turner, J. A. Relationship between Q-factor and sample damping for contact resonance atomic force microscope measurement of viscoelastic properties. *J. Appl. Phys.* **2011**, *109*, 113528−5.

(29) Van Landingham, M. R.; Drzal, P. L.; White, C. C. Indentation creep and relaxation measurements of polymers. *Mater. Res. Soc. Symp. Proc.* **2005**, *841*, 193−204.

(30) Fischer-Cripps, A. C. A simple phenomenological approach to nanoindentation creep. *Mater. Sci. Eng., A* **2004**, *385*, 74−82.

(31) Ferry, J. D. Viscoelastic Properties of Polymers; Wiley: New York, 1961.

(32) Weisenhorn, A. L.; Hansma, P. K.; Albrecht, T. R.; Quate, C. F. Forces in atomic force microscopy in air and water. *Appl. Phys. Lett.* **1989**, *54*, 2651−2653.

(33) Cappella, B.; Dietler, G. Force-distance curves by atomic force microscopy. *Surf. Sci. Rep.* **1999**, *34*, 1−104.

(34) Haugstad, G. *Atomic Force Microscopy: Understanding Basic Modes and Advanced Applications*; Wiley: Hoboken, NJ, 2012.

(35) Chizhik, S. A.; Huang, Z.; Gorbunov, V. V.; Myshkin, N. K.; Tsukruk, V. V. Micromechanical properties of elastic polymeric materials as probed by scanning force microscopy. *Langmuir* **1998**, *14*, 2606−2609.

(36) Hertz, H. Ueber die Berührung fester elastischer Körper. *J. Reine Angew. Math.* **1882**, *92*, 156−171.

(37) Sneddon, I. N. The relation between load and penetration in the axisymmetric boussinesq problem for a punch of arbitrary profile. *Int. J. Eng. Sci.* **1965**, *3*, 47−57.

(38) Rico, F.; Roca-Cusachs, P.; Gavara, N.; Farre, R.; Rotger, M.; Navajas, D. Probing mechanical properties of living cells by atomic force microscopy with blunted pyramidal cantilever tips. *Phys. Rev. E* **2005**, *72*, 021914−10.

(39) Bradley, R. S. The cohesive force between solid surfaces and the surface energy of solids. *Philos. Mag.* **1932**, *13*, 853−862.

(40) Drelich, J.; Mittal, K. L. *Atomic Force Microscopy in Adhesion Studies*; Taylor & Francis: Boston, 2005.

(41) Johnson, K. L.; Greenwood, J. A. An adhesion map for the contact of elastic spheres. *J. Colloid Interface Sci.* **1997**, *192*, 326−333.

(42) Schwarz, U. D. A generalized analytical model for the elastic deformation of an adhesive contact between a sphere and a flat surface. *J. Colloid Interface Sci.* **2003**, *261*, 99−106.

(43) Carpick, R. W.; Ogletree, D. F.; Salmeron, M. A general equation for fitting contact area and friction vs load measurements. *J. Colloid Interface Sci.* **1999**, *211*, 395−400.

(44) Tabor, D. *The Hardness of Metals*; Clarendon Press: Oxford, England, 1951.

(45) Fischer-Cripps, A. C. Critical review of analysis and interpretation of nanoindentation test data. *Surf. Coat. Technol.* **2006**, *200*, 4153−4165.

(46) Balasundaram, K.; Raabe, D.; Cao, Y. Identifying the limitation of Oliver and Pharr method in characterizing the viscoelasticplastic materials with respect to indenter geometry. *Mater. Res. Soc. Symp. Proc.* **2008**, *1137*, 49−54.

(47) Van Landingham, M. R.; Chang, N. K.; Drzal, P. L.; White, C. C.; Chang, S. H. Viscoelastic characterization of polymers using instrumented indentation. I. Quasi-static testing. *J. Polym. Sci., Part B: Polym. Phys.* **2005**, *43*, 1794−1811.

(48) Moeller, G. AFM nanoindentation of viscoelastic materials with large end-radius probes. *J. Polym. Sci., Part B: Polym. Phys.* **2009**, *47*, 1573−1587.

(49) Braunsmann, C.; Proksch, R.; Revenko, I.; Schäffer, T. E. Creep compliance mapping by atomic force microscopy. *Polymer* **2014**, *55*, 219−225.

(50) Baro, A.; Reifenberger, R. *Atomic Force Microscopy in Liquid: Biological Applications*; Wiley-VCH: Weinheim, Germany, 2012.

(51) Garcia, R.; Herruzo, E. T. The emergence of multifrequency force microscopy. *Nat. Nano.* **2012**, *7*, 217−226.

(52) Hurley, D. Contact Resonance Force Microscopy Techniques for Nanomechanical Measurements. In *Applied Scanning Probe Methods XI*; Springer: Berlin, 2009.

(53) Zhou, X.; Fu, J.; Li, F. Contact resonance force microscopy for nanomechanical characterization: Accuracy and sensitivity. *J. Appl. Phys.* **2013**, *114*, 064301−13.

(54) Yablon, D. G. *Scanning Probe Microscopy for Industrial Applications: Nanomechanical Characterization*; Wiley: Hoboken, NJ, 2013.

(55) Tsukruk, V. V. Scanning probe microscopy of polymer surfaces. *Rubber Chem. Technol.* **1997**, *70*, 430−467.

(56) Hazel, J.; Tsukruk, V. V. Spring constants of composite ceramic/gold cantilevers for scanning probe microscopy. *Thin Solid Films* **1999**, *339*, 249−257.

(57) Tsukruk, V. V.; Huang, Z. Micro-thermomechanical properties of heterogeneous polymer films. *Polymer* **2000**, *41*, 5541−5545.

(58) Tsukruk, V. V.; Huang, Z.; Chizhik, S. A.; Gorbunov, V. V. Probing of micromechanical properties of compliant polymeric materials. *J. Mater. Sci.* **1998**, *33*, 4905−4909.

(59) Tsukruk, V. V.; Sidorenko, A.; Gorbunov, V. V.; Chizhik, S. A. Surface nanomechanical properties of polymer monolayers with domain structure. *Langmuir* **2001**, *17*, 6715−6719.

(60) McConney, M. E.; Singamaneni, S.; Tsukruk, V. V. Probing soft matter with the atomic force microscope: force-spectroscopy and beyond. *Polym. Rev.* **2010**, *50*, 235−286.

(61) Tsukruk, V. V.; Reneker, D. H. Scanning probe microscopy of polymeric and organic molecular films: from self-assembled monolayers to composite multilayers. *Polymer* **1995**, *36*, 1791−1808.

(62) Tsukruk, V. V.; Sidorenko, A.; Yang, H. Polymer nanocoatings with non-linear elastic response. *Polymer* **2002**, *43*, 1650−1695.

(63) Julthongpiput, D.; LeMieux, M.; Tsukruk, V. V. Micromechanical properties of glassy and rubbery polymer brush layers as probed by atomic force microscopy. *Polymer* **2003**, *44*, 4557−4562.

(64) LeMieux, M. C.; Peleshanko, S.; Anderson, K. D.; Tsukruk, V. V. Adaptive nanomechanical response of stratified polymer brush structures. *Langmuir* **2007**, *23*, 265−273.

(65) Choi, T.; Jang, J.-H.; Ullal, C. K.; Lemieux, M. C.; Tsukruk, V. V.; Thomas, E. L. The elastic properties and plastic behavior of two-dimensional polymer structures fabricated with laser interference lithography. *Adv. Funct. Mater.* **2006**, *16*, 1324−1330.

(66) Shulha, H.; Zhai, X.; Tsukruk, V. V. Molecular stiffness of individual dendritic macromolecules and their aggregates. *Macromolecules* **2003**, *36*, 2825−2831.

(67) Peleshanko, S.; Julian, M. D.; Ornatska, M.; McConney, M. E.; LeMieux, M. C.; Chen, N.; Tucker, C.; Yang, Y.; Liu, C.; Humphrey, J. A. C.; Tsukruk, V. V. Hydrogel-encapsulated microfabricated haircells mimicking fish cupula neuromasts. *Adv. Mater.* **2007**, *19*, 2903−2909.

(68) Ye, C.; Drachuk, I.; Calabrese, R.; Dai, H.; Kaplan, D. L.; Tsukruk, V. V. Permeability and micromechanical properties of silk ionomer microcapsules. *Langmuir* **2012**, *28*, 12235−12244.

(69) Cook, S. M.; Schaffer, T. E.; Chynoweth, K. M.; Wigton, M.; Simmonds, R. W.; Lang, K. M. Practical implementation of dynamic methods for measuring atomic force microscope cantilever spring constants. *Nanotechnology* **2006**, *17*, 2135−2145.

(70) Tsukruk, V. V.; Gorbunov, V. V.; Huang, Z.; Chizhik, S. A. Dynamic microprobing of viscoelastic polymer properties. *Polym. Int.* **2000**, *49*, 441−444.

(71) Keller, D. Reconstruction of STM and AFM images distorted by finite-size tips. *Surf. Sci.* **1991**, *253*, 353−364.

(72) Sedin, D. L.; Rowlen, K. L. Adhesion forces measured by atomic force microscopy in humid air. *Anal. Chem.* **2000**, *72*, 2183−2189.

(73) Lin, D. C.; Dimitriadis, E. K.; Horkay, F. Robust strategies for automated AFM force curve analysis − I. Non-adhesive indentation of soft, inhomogeneous materials. *J. Biomech. Eng.* **2006**, *129*, 430−440.

(74) D Tranchida, D.; Kiflie, Z.; Acierno, S.; Piccarolo, S. Nanoscale mechanical characterization of polymers by atomic force microscopy (AFM) nanoindentations: viscoelastic characterization of a model material. *Meas. Sci. Technol.* **2009**, *20*, 095702−9.

(75) Child, W. C., Jr; Ferry, J. D. Dynamic mechanical properties of poly-n-butyl methacrylate. *J. Colloid Interface Sci.* **1957**, *12*, 327−341.

(76) Williams, M. L.; Landel, R. F.; Ferry, J. D. The temperature dependence of relaxation mechanisms in amorphous polymers and other glass-forming liquids. *J. Am. Chem. Soc.* **1955**, *77*, 3701−3707.

(77) Shulha, H.; Kovalev, A.; Myshkin, N.; Tsukruk, V. V. Some aspects of AFM nanomechanical probing of surface polymer films. *Eur. Polym. J.* **2004**, *40*, 949−956.

(78) Tschoegl, N. W. *The Phenomenological Theory of Linear Viscoelastic Behavior: An Introduction*; Springer-Verlag: Berlin, 1989.

(79) Johnson, K. L. Contact mechanics and adhesion of viscoelastic spheres. *ACS Symp. Ser.* **2000**, *741*, 24−41.

(80) Chatterjee, S.; Hadi, A. S. *Regression Analysis by Example*; Wiley: Hoboken, NJ, 2013.

(81) Teixeira, S. S.; Dias, C. J.; Dionisio, M.; Costa, L. C. New method to analyze dielectric relaxation processes: a study on polymethacrylate series. *Polym. Int.* **2013**, *62*, 1744−1749.

(82) Meier, G.; Fytas, G.; Dorfmueller, T. Photon correlation study of the relaxation processes in bulk poly(n-butyl methacrylate). *Macromolecules* **1984**, *17*, 957−961.

(83) Tschoegl, N. W.; Emri, I. Generating line spectra from experimental responses. Part II: Storage and loss functions. *Rheol. Acta* **1993**, *32*, 322−327.

(84) Kaliappan, S. K. Characterization of Physical Properties of Polymers Using AFM Force Distance Curves. Ph.D. Dissertation, Siegen University, 2007.